4 Retrieval– Principle and Method

4.1 Retrieval Algorithm

4.1.1 Principle of Limb Sounding Instruments

Microwave limb sounding instruments obtain remote measurements of atmospheric parameters by observing thermal emission at millimeter and sub-millimeter-wavelength as the instrument field of view (FOV) is scanned through the atmosphere. Limb sounding means that the atmosphere is observed tangentially, as schematically shown in Figure 4.1.

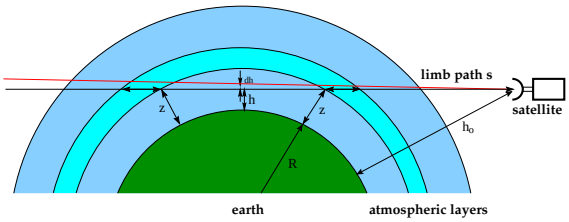

Figure 4.1 Illustration of limb sounding geometry. The satellite is in orbit and looks tangentially through the atmosphere. The beam is lowest at the tangent point at an altitude h.

The intensity detected by satellite observation contains implicit information about the parameters of interest. The extraction of these parameters from the satellite measurement requires knowledge of the radiative transfer in the atmosphere. The radiative transfer equation, introduced by Chandrasekhar [*Chandrasekhar*, 1960], describes the way in which the intensity is affected by extinction and emission of radiation. The intensity, I, is defined as the power of radiation per unit area, per unit solid angle, and per unit frequency interval (measured in $\mathrm{Wm^{-2}sr^{-1}Hz^{-1}}$). In the case of a non-scattering atmosphere (clear sky), for an arbitrary slant path, the intensity I at frequency ν received by an instrument at position $s = 0$ is given by :

$$I(\nu) \quad = \quad I_\infty(\nu)\zeta(\infty,\nu) + \int_0^\infty k(s,\nu)B(\nu,T(s))\zeta(s,\nu)ds \tag{4.1}$$

where k is the total absorption coefficient (the SI unit for k is $\mathrm{m^{-1}}$), ζ is the transmittance, B is the Planck function (which is derived under thermodynamic equilibrium condition), and I_∞ is the intensity at the limit of the atmosphere, which is cosmic background radiation or emission from the ground. The meaning of these quantities is explained below. Equation 4.1 is schematically shown in Figure 4.2.

For a mixture of gases the total absorption coefficient (summed over all the species) is given by:

$$k = \sum_i n_i \sigma_i \tag{4.2}$$

where n_i is the number density of species i (measured in $\mathrm{m^{-3}}$), and σ_i is the absorption cross section (measured in $\mathrm{m^2}$).

The optical depth (or opacity) τ, between an initial point s_0 and a final point s is defined as:

$$\tau(s,\nu) = \int_{s_0}^{s} k(s,\nu)ds \tag{4.3}$$

and the transmittance ζ is defined as:

$$\zeta(s,\nu) = \exp(-\tau(s,\nu)) \tag{4.4}$$

The Planck function describes the intensity which a perfect blackbody at temperature T emits, and is defined as:

$$B(\nu, T) = \frac{2h\nu^3}{c^2(\exp(h\nu/k_B T) - 1)} \tag{4.5}$$

where h is Planck's constant, k_B is Boltzmann's constant, and c is the speed of light. $B(\nu, T)$ has the same units as $I(\nu, T)$, i.e. $\mathrm{Wm^{-2}sr^{-1}Hz^{-1}}$.

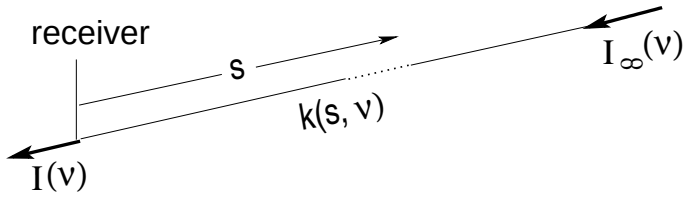

Figure 4.2 Schematic display of the geometry for remote sensing of the atmosphere.

The atmospheric radiative transfer is simulated by a computer model, called forward model $\mathbf{F}$, using a limited number of parameters as input. The calculation of the absorption coefficients (Equation (4.2)) and the integration of the radiative transfer equation (Equation (4.1)) are performed for a single frequency and a pencil beam, respectively, while both the spectrometer channels and antenna pattern are not infinitely narrow. Therefore a convolution between the signal from the atmosphere as a function of frequency and the spectrometer channel shape, and between the signal as a function of viewing direction and the antenna pattern, is required. Thus, the observed signal becomes a vector y, which can be expressed as:

$$\mathsf{y} = \mathbf{F}(\mathsf{x}, \mathsf{b}) + \epsilon \tag{4.6}$$

where (x, b) gives a total description of both the atmospheric and sensor states, and ϵ is the measurement noise. The x vector contains all the parameter to be retrieved, while the vector b contains the model parameters. For a heterodyne instrument, as is the case of the SMILES instrument, the most important sensor parts are the antenna, the mixer, the sideband filter and the spectrometer.

4.1.2 Retrieval Method and Basic Error Estimation

Including the measurement noise $\boldsymbol{\epsilon} = {}^T(\epsilon_1, \epsilon_2, \cdots, \epsilon_m)$, the observation equation is expressed by

$$\mathbf{y} = \mathbf{F}(\mathbf{x}) + \boldsymbol{\epsilon}. \tag{4.7}$$

Here we omit the model parameters appearing in the forward model for simplicity.

In general the forward function $\mathbf{F}$ is nonlinear with respect to the state vector but the linear approximation is expected to be reasonable for most target gases of SMILES. In this assumption, it is natural to expand the forward function around the *a priori* value $\mathbf{x}_a$,

$$\mathbf{y} \approx \mathbf{F}(\mathbf{x}_a) + \mathbf{K}_x(\mathbf{x} - \mathbf{x}_a) + \boldsymbol{\epsilon}, \tag{4.8}$$

$$\mathbf{K}_x = \left.\frac{\partial \mathbf{F}(\mathbf{x})}{\partial \mathbf{x}}\right|_{\mathbf{x}_a}. \tag{4.9}$$

The retrieval method which we adopt is the optimal estimation method [*Rodgers*, 1976]. The optimal linear solution can be given by

$$\hat{\mathbf{x}} = \mathbf{x}_a + \mathbf{D}_y \left[\mathbf{y} - \mathbf{F}(\mathbf{x}_a)\right], \tag{4.10}$$

where the contribution function is

$$\begin{aligned} \mathbf{D}_y &= (\mathbf{K}_x^T \mathbf{S}_\epsilon^{-1} \mathbf{K}_x + \mathbf{S}_a^{-1})^{-1} \mathbf{K}_x^T \mathbf{S}_\epsilon^{-1}, & (4.11)\\ &= \mathbf{S}_a \mathbf{K}_x^T (\mathbf{K}_x \mathbf{S}_a \mathbf{K}_x^T + \mathbf{S}_\epsilon)^{-1}, & (4.12) \end{aligned}$$

and $\mathbf{S}_\epsilon$ and $\mathbf{S}_a$ are the measurement error covariance matrix and the *a priori* error covariance matrix, respectively. It is also possible to express the retrieval in terms of the averaging kernel matrix

$$\mathbf{A} \equiv \frac{\partial \hat{\mathbf{x}}}{\partial \mathbf{x}} = \mathbf{D}_y \mathbf{K}_x, \tag{4.13}$$

as follows:

$$\hat{\mathbf{x}} = (\mathbf{I} - \mathbf{A})\mathbf{x}_a + \mathbf{A}\mathbf{x} + \mathbf{D}_y \boldsymbol{\epsilon}. \tag{4.14}$$

Finally, the retrieval error covariance is given by

$$\begin{aligned} \mathbf{S} &= (\mathbf{A} - \mathbf{I}_n)\mathbf{S}_a(\mathbf{A} - \mathbf{I}_n)^T + \mathbf{D}_y \mathbf{S}_\epsilon \mathbf{D}_y^T, & (4.15)\\ &= (\mathbf{K}_x^T \mathbf{S}_\epsilon^{-1} \mathbf{K}_x + \mathbf{S}_a^{-1})^{-1}. & (4.16) \end{aligned}$$

The comprehensive error analysis including the model parameters is found in the original literature [*Rodgers*, 1990].

4.2 Simulation of Observation Spectra

We have two simulators available for analyses of the SMILES observations. One is SMOCO (SMILES Observation retrieval Code) developed by the CRL, and the other is ARTS (Atmospheric Radiative Transfer Simulator) by the Institute of Remote Sensing, University of Bremen, Germany, and the Chalmers University, Göteborg, Sweden. These simulators are capable to produce emission spectra of the SMILES observations by the use of atmospheric and instrumental knowledge. They can also calculate the weighting functions. These are essential quantities used to expand the observation equation into a linear relation in the optimal estimation method. Since the simulation model is the basis for the correct retrieval of atmospheric species from the limb sounding measurements, we conducted intercomparisons between the two simulation models. SMOCO and ARTS have basically generated the same spectra. The results are also given in this section.

4.2.1 ARTS Forward Model

Forward models consist of either empirically determined relationships or numerical counterparts of the physical relationships needed to describe the radiative transfer and sensor effects. The ARTS is mainly of the latter type, but some parts are more based on empirical investigations, such as the parameterizations of continuum absorption.

The ARTS forward model is separated into two parts: atmospheric part and sensor part. Thus, the state vector x and forward model parameter vector b are expressed as:

$$\mathsf{x} = \begin{pmatrix} \mathsf{x}_r \\ \mathsf{x}_s \end{pmatrix} \tag{4.17}$$

and

$$\mathsf{b} = \begin{pmatrix} \mathsf{b}_r \\ \mathsf{b}_s \end{pmatrix}, \tag{4.18}$$

respectively, where $(\mathsf{x}_r, \mathsf{b}_r)$ refers to the atmospheric part, and $(\mathsf{x}_s, \mathsf{b}_s)$ refers to the sensor part.

4.2.1.1 Atmospheric Part

The first part describes the atmospheric radiative transfer, independent of the sensor characteristics, i.e., for pencil beam (infinite spatial resolution) monochromatic (infinite frequency resolution) signals. The intensity i of the signal received from the atmosphere is expressed by:

$$\mathsf{i} = \mathbf{F}_a(\mathsf{x}_r, \mathsf{b}_r) \tag{4.19}$$

Practically, to calculate i (by solving the radiative transfer equation), the line of sight (LOS) is divided into n equidistant points (distance noted with Δl). The absorption and transmission is assumed to vary linearly between the points. The optical depth τ_i, associated with the step i is calculated as:

$$\tau_i = \frac{\Delta l}{2}\left(k_i + k_{i+1}\right), \quad 1 \leq i < n \tag{4.20}$$

where k_i and k_{i+1} are the absorption coefficients calculated at the i^{th} and $(i+1)^{th}$ LOS points, respectively.

The transmission associated with step i is:

$$\zeta_i = \exp(-\tau_i), \quad 1 \leq i < n \tag{4.21}$$

The absorption coefficients are calculated at the LOS points, from the absorption matrix, calculated on a logarithmic pressure grid, by linear interpolation. The grid for the calculation of the absorption matrix does not necessarily contain the corresponding grid points of the LOS.

The source function S_i is assumed to vary linearly between the LOS points, but for simplicity, a single source function value S_i is assigned to each LOS point, i.e.,:

$$S_i = \frac{S_i + S_{i+1}}{2}, \quad 1 \leq i < n \tag{4.22}$$

The intensity at the point n, i.e. at the end of LOS, is computed using the following iterative expression:

$$\mathsf{i}_{i+1} = \mathsf{i}_i\zeta_i + S_i\left(1 - \zeta_i\right), \quad 1 \leq i < n-1 \tag{4.23}$$

where i_i is the intensity reaching point i. The iteration starts by setting i_1 to the cosmic background radiation.

4.2.1.2 Sensor Part

The second part takes into account the sensor characteristics, such as the measurement vector is given by:

$$\mathsf{y} = \mathbf{F}_s(\mathsf{i}, \mathsf{x}_s, \mathsf{b}_s) + \epsilon_{\mathsf{y}} \tag{4.24}$$

where the i is the vector holding the spectral values of the signal emitted by the atmosphere for a set of considered frequencies, and viewing directions (calculated as described

above). For a heterodyne instrument, as is the case of millimeter/sub-millimeter limb sounding instruments, the most important sensor parts are the antenna, the mixer, the sideband filter and the spectrometer. Therefore, the modeling of the sensor part is either a summation of different frequencies (mixer), or it is a convolution of the spectra as a function of frequency (spectrometer) or as a function of viewing direction (antenna) with the characteristic instrument response functions of concern. Summation and weighting of the spectral components are both linear operations, and thus it is possible to model the effects of the different sensor parts as subsequent matrix multiplications of the monochromatic pencil beam spectrum [*Eriksson*, 2001]:

$$\mathsf{y} = \mathsf{H}_n \cdots \mathsf{H}_2 \mathsf{H}_1 \mathsf{i} + \epsilon_{\mathsf{y}} \tag{4.25}$$

where n is the total number of the considered sensor components, and H_i $(1 \leq i \leq n)$ is the sensor matrix corresponding to the i^{th} component of the sensor. Thus, the sensor model can be implemented as a straightforward matrix multiplication and the measurement vector is given by:

$$\mathsf{y} = \mathsf{H}\mathsf{i} + \epsilon_{\mathsf{y}} \tag{4.26}$$

where $\mathsf{H} = \mathsf{H}_n \cdots \mathsf{H}_2 \mathsf{H}_1$.

The big advantage of this implementation is that the sensor matrix H is constant for a specific instrument, and it can be stored for further calculations.

4.2.1.3 Weighting Function

The separation of the forward model in two parts, the atmospheric part and the sensor part, is very important for the practical calculation of the weighting function. Thus the weighting function, representing the sensitivity of the measurement to the state vector x, can be written as:

$$\mathsf{K}_{\mathsf{x}} = \frac{\partial \mathsf{y}}{\partial \mathsf{x}} = \frac{\partial \mathsf{y}}{\partial \mathsf{i}} \frac{\partial \mathsf{i}}{\partial \mathsf{x}} = \mathsf{H} \frac{\partial \mathsf{i}}{\partial \mathsf{x}} \tag{4.27}$$

Thus the new parts needed to calculate atmospheric weighting functions, are function giving $\partial \mathsf{i}/\partial \mathsf{x}$, where x is the state vector representing a VMR profile, or temperature profile, or spectroscopic data, etc.

The weighting functions can be calculated analytically, or numerically. In ARTS the weighting functions are in general calculated analytically (e.g., for the VMR profiles) but there are some exceptions (e.g., for the atmospheric temperature profile when the hydrostatic equilibrium is assumed, or for the pointing offset) when they are calculated numerically.

4.2.2 SMOCO Forward Model

SMOCO and ARTS share purposes and basic functions. The SMOCO forward model also comprises two components, i.e., atmospheric part and sensor one. These are constructed in principle according to the same method as described for ARTS. Therefore, the following descriptions are focused mainly on aspects characteristic to SMOCO.

4.2.2.1 Atmospheric Part

The atmospheric part of SMOCO calculates molecular absorption coefficients by a line-by-line method, and numerically solves radiative transfer equations for the limb atmosphere. SMOCO has taken emission-line frequencies from the JPL catalog [*Pickett et al.*, http://spec.jpl.nasa.gov/], and parameters for pressure broadening and pressure shifts from

the HITRAN data or other published information. The absorption by water vapor and the continuum emissions are calculated by Liebe's millimeter-wave propagation model (MPM93)[*Liebe*, 1993]. SMOCO takes into account atmospheric refraction when it solves radiative transfer equations. The refraction is significant for lower altitudes as shown in Section 3.2.1.6. SMOCO is capable to deal with an asymmetric atmosphere that has different molecular mixing ratios in farther and nearer regions from the tangent point along the line of sight. This function is effective to improve a horizontal resolution in the direction if needed.

4.2.2.2 Sensor Part

In the sensor part, SMOCO deals with instrumental effects including the antenna radiation pattern, receiver sidebands, Doppler shift of frequency, and AOS frequency response function.

Antenna Radiation Pattern

The antenna will receive radiation signals that come to the aperture in an extended solid angle around the optical axis. Such response is expressed by the antenna radiation pattern, which is modeled in Section 3.2.4 for the SMILES antenna. The signal power received by the antenna is given by a spatial integration of the atmospheric brightness distribution weighted with the antenna radiation pattern. The main beam in the radiation pattern is often described by its half-power beam-width (HPBW). The HPBW of the SMILES antenna will be 0.08° (in elevation) and 0.16° (in azimuth). The spatial integration will cover the main beam and its surrounding area within a diameter of 2.5 times the HPBW. We call this area a field of view (FOV) for SMILES observations. However, we cannot completely neglect the power contribution from the outside of the FOV. The SMILES design assumes that the integration of the antenna radiation pattern within the FOV be higher than 85 % of the whole integration over 4π steradian. SMOCO takes into account these effects when it calculates the signal power received by the antenna.

Receiver Sidebands

Since the submillimeter mixer, including SMILES' SIS mixer, is sensitive to both sidebands, the receiver output is proportional to the combined RF power from the upper sideband (USB) and lower sideband (LSB). This means that the atmospheric emissions in one sideband (signal band) are superimposed on those from the other sideband (image band). However, thanks to a single sideband (SSB) filter, SMILES can suppress the image-band levels lower than 1 percent as shown in Section 3.3.2.2. SMOCO calculates the frequency down-conversion by the submillimeter receiver associated with the SSB filter.

Doppler Shift of Frequency

SMOCO deals with the Doppler shift of frequency caused by the movement of the ISS and the rotation of the Earth. The shift due to the ISS motion is some 10 MHz, depending on yaw deviations in the SMILES attitude. The shift due to the Earth rotation is about 1.5 MHz at most, while the effect is larger when the ISS flies toward the south compared with the case toward the north. Since the direction of the frequency shift for the LSB and USB is opposite in the IF domain, the effect is to be calculated prior to the down conversion in the forward model. Furthermore, the effect has to be properly taken into

account when some daily or weekly averaged data are simulated and used in the retrieval process.

Acousto-Optical Spectrometer (AOS)

First, each channel of the AOS has a Gaussian-like frequency response function as shown in Section 3.3.3.1. By integrating original real spectra with the weighting function, SMOCO simulates the AOS output that is separated in channels. Secondly, since the exact frequency of each channel is sensitive to the environment temperatures, SMILES measures the frequency-channel relation in every 53 seconds with a reference signal onboard. The relation is to be used in the calculation of the AOS output.

4.2.2.3 Weighting Function

The variation in the brightness temperature observed at a tangent height can be expressed by a linear combination of variations in the molecular volume-mixing ratio, pressure, temperature, and the error in the tangent height determination of each observation.

$$\Delta T_A = \int_{z_{min}}^{z_{max}} \left\{ \sum_i K_i \Delta x_i + K_p \Delta(\ln P) + K_T \Delta T \right\} \mathrm{d}z + K_{HT} \Delta z_0. \tag{4.28}$$

Each weighting function is therefore given by

$$K_i = \frac{\partial T_A}{\Delta z \partial x_i}, \quad K_P = \frac{\partial T_A}{\Delta z \partial \ln P}, \quad K_T = \frac{\partial T_A}{\Delta z \partial T}, \quad K_{HT} = \frac{\partial T_A}{\partial z_0}, \tag{4.29}$$

where z_0 is the tangent height of the antenna beam axis. SMOCO evaluates the weighting functions by analytic expressions, but does the tangent height errors from numerical differences,

$$K_{HT} = \frac{T_A(z_0 + \Delta z_0) - T_A(z_0)}{\Delta z_0}. \tag{4.30}$$

4.2.3 Forward Model Intercomparison

An intercomparison was carried out between the results produced by two forward models, SMOCO and ARTS. This concerned both the computation of absorption coefficients and integration of radiative transfer.

The intercomparison calculations were performed using a number of input parameters predefined by the ARTS developers.

Absorption Coefficient Intercomparison

In order to check the model implementation for line absorption calculations, line-by-line calculations were carried out. Absorption coefficients were computed for a large number of frequencies in a variety of spectral ranges where important molecular species have signatures. The considered spectral ranges were about 1 GHz wide, and centered on the set of selected molecular species spectral transitions listed in Table 4.1. A set of spectroscopic parameters for each considered transition was defined by the ARTS developers, including the line center frequency, the line intensity, the lower state energy, and the pressure

species	line center frequency	species	line center frequency
H_2O	22.2 GHz	N_2O	502 GHz
O_3	110.83 GHz	HNO_3	544 GHz
O_2	118.7 GHz	CO	576 GHz
H_2O	183.3 GHz	O_3	625.37 GHz
HCN	354 GHz	HCl	625.9 GHz
ClO	501 GHz	ClO	649.45 GHz

Table 4.1 Selected molecular species transitions for the absorption coefficients intercomparison.

broadening parameters. The provided spectroscopic data was based on the HITRAN catalog [*Rothman et al.*, 1992]. The Voigt lineshape was selected to compute the absorption coefficients. The polynomial coefficients used to compute the partition function, and the isotopic ratio for each isotope of each target species were also provided. In addition to the spectroscopic data, provided were the atmospheric temperature and pressure profile, and the VMR profiles of the selected molecular species.
The spectra of the absorption coefficients were calculated for atmospheric levels ranging from 0 to 60 km, for the full set of considered spectral lines in one run. That means that the possible contributions from the strong lines far away from the watched spectral range are also included.

The results of the intercomparison showed that there is a good agreement between the two models. With a few exceptions for some spectral ranges the relative differences between the models are less than 1%. Here we present only some results for a set of spectral ranges around some transitions mainly of interest for the SMILES study:

- H_2O at 22.23 GHz, a transition of great interest for microwave radiometry.
- O_3 at 625.37 GHz, the transition observed by the SMILES instrument (in Band A and Band B).
- HCl at 625.9 GHz, observed by the SMILES instrument (in Band B).
- ClO at 649.45 GHz, a transition of great interest for microwave radiometry . This emission will also be observed by the SMILES instrument (in Band C).

The two models are very close to each other. In the frequency range around the H_2O line emission a relative difference of less than 0.015% is found (Figure 4.3, lower plot). Similar results are obtained for the spectral range around 625.37 GHz (Figure 4.4, lower plot). In the spectral range around 626.9 GHz (Figure 4.5, lower plot) the relative differences between the two models are about 1%. The differences appear to be caused by the pressure shift, which seems to be not taken into account in the SMOCO model. An offset between the two calculations appear in the spectral range around the ClO transition at 649.45 GHz (Figure 4.6, lower plot). This offset seems to be caused by a baseline due to other line species absorption, as at this altitudes the emission signal from ClO is almost negligible (see Figure 4.6, upper plot).

Radiative Transfer Intercomparison

The intercomparison at the stage presented here aimed to investigate the differences between the models due solely to the numerical solution of the radiative transfer equation. A

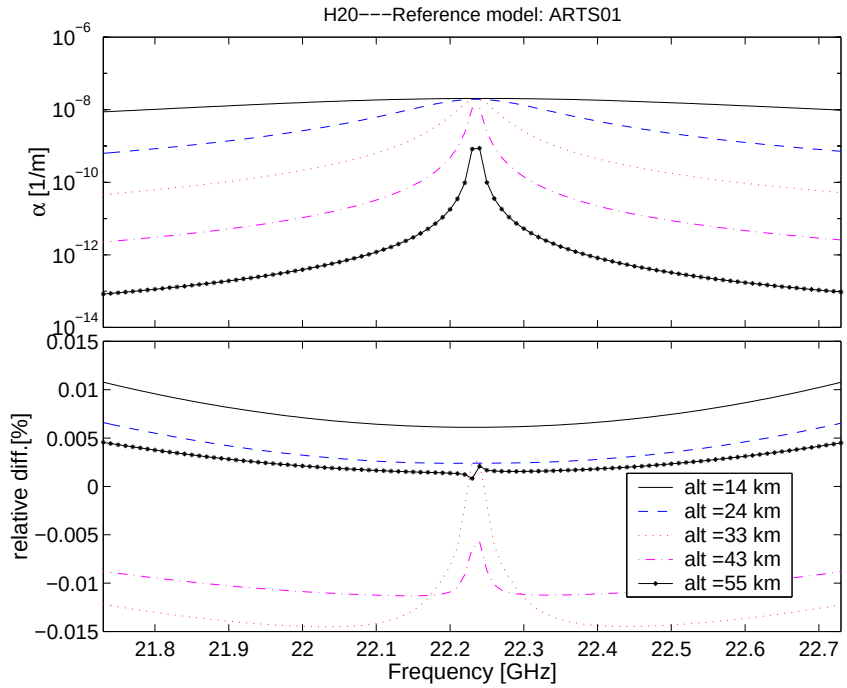

Figure 4.3 Upper: ARTS calculations of the absorption spectra in the frequency range around the H_2O line at 22.23 GHz for different atmospheric levels. Lower: Relative difference between the absorption spectra calculated with the two models SMOCO and ARTS. The ARTS model was taken as a reference model.

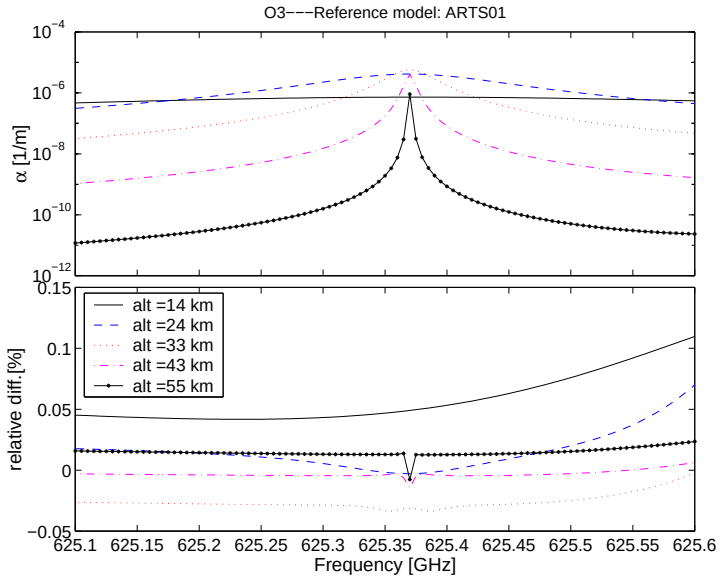

Figure 4.4 Upper: ARTS calculations of the absorption spectra in the frequency range around the O_3 line at 625.37 GHz for different atmospheric levels. Lower: Relative difference between the absorption spectra calculated with the two models SMOCO and ARTS. The ARTS model was taken as a reference model.

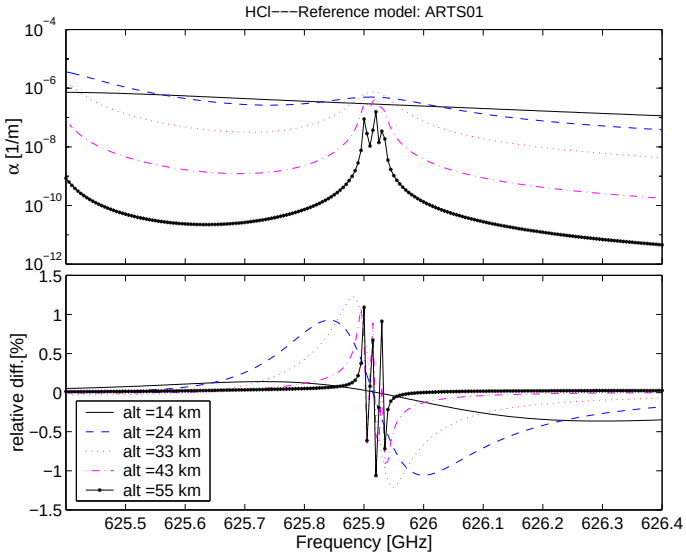

Figure 4.5 Upper: ARTS calculations of the absorption spectra in the frequency range around the HCl line at 625.9 GHz for different atmospheric levels. Lower: Relative difference between the absorption spectra calculated with the two models SMOCO and ARTS. The ARTS model was taken as a reference model.

standard set of absorption coefficient spectra, calculated on a fine vertical grid, was provide by the ARTS developers. These absorption spectra were used the provide the brightness temperature for a set of viewing direction. The other necessary specifications, such as the platform altitude, were also provided. The brightness temperature spectra seen by a limb looking instrument under a set of viewing angle, and the absolute difference between the SMOCO and ARTS calculations are displayed in Figure 4.7. An absolute deviation of about 1 K appears in the line wings (Figure 4.7, lower plot). The deviations in the line center are almost negligible.

4.2.4 Observational Spectra Simulated by SMOCO

JEM/SMILES has three frequency bands: Band-A; 624.32 – 625.52 GHz, Band-B; 625.12 – 626.32 GHz, and Band-C; 649.12 – 650.32 GHz. Figure 4.8 shows an example of the SMILES spectra for the three frequency bands at a tangent height of 40 km. These spectra are expected with an averaging of 30 atmospheric scans in orbit, which correspond to a half-day (12 hour) zonal mean averaged over a 5° latitude-width in the mid-latitude.

In the above simulations SMOCO was used with settings as follows.

- We used an antenna response pattern including wide-angle sidelobes with a beam efficiency of 0.85, which is described in section 3.2.4 of this Mission Plan.
- The ISS altitude is assumed to be its nominal value 407 km.
- The model atmospheres at latitudes of 0°N, 45°N, and 80°N are of the Rutherford Appleton Laboratory, which include molecular concentrations, temperatures, pressures from 0 to 120 km.
- The center frequencies of molecules used in SMOCO are shown in Table 4.2.

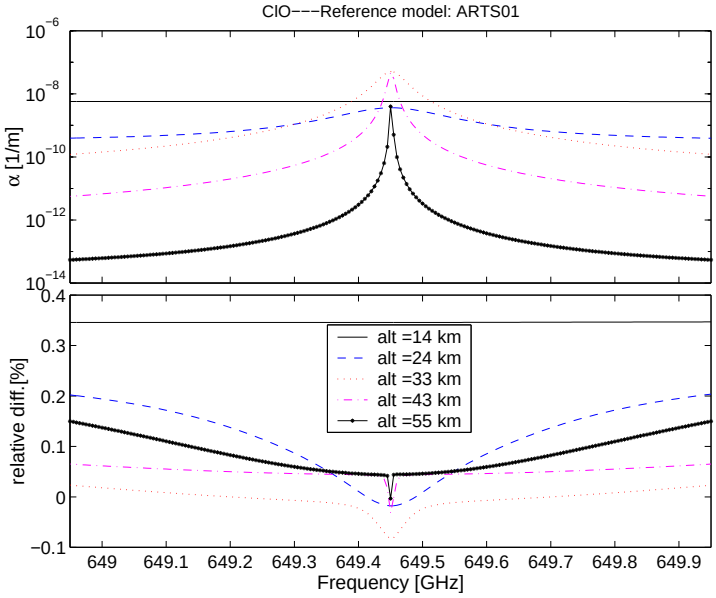

Figure 4.6 Upper: ARTS calculations of the absorption spectra in the frequency range around the ClO line at 649.45 GHz for different atmospheric levels. Lower: Relative difference between the absorption spectra calculated with the two models SMOCO and ARTS. The ARTS model was taken as a reference model.

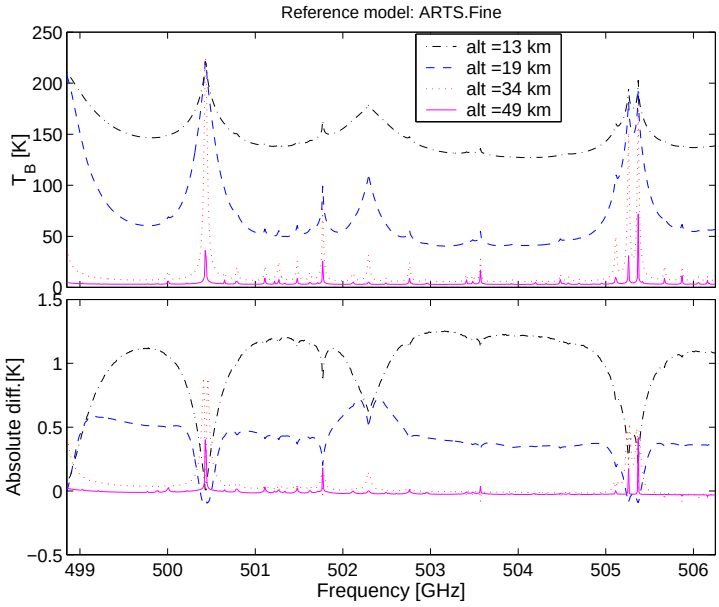

Figure 4.7 Upper: Arts calculations of brightness temperature spectra seen by a limb sounding instrument. Lower: Absolute difference between brightness temperatures calculated with the two models (SMOCO and ARTS) calculation. The ARTS model was taken as a reference model.

Table 4.2 Molecular transition frequencies of JEM/SMILES species.

BAND A (GHz)		*BAND B* (GHz)		*BAND C* (GHz)	
624.32-625.52 GHz		625.12 - 626.32 GHz		649.12 - 650.32 GHz	
HNO_3	624.48				
CH_3CN	624.50				
CH_3CN	624.63				
CH_3CN	624.73	$HO^{81}Br$	625.18		
^{81}BrO	624.77	O_3 (v_2)	625.28	^{18}OOO	649.14
HNO_3	624.78	O_3 (v_2)	625.32	^{17}OOO	649.14
CH_3CN	624.82	$HO^{79}Br$	625.33	^{18}OOO	649.15
OClO	624.82	HNO_3	625.34	^{17}OOO	649.27
$O^{18}OO$	624.83	O_3	625.37	^{17}OOO	649.38
$ClONO_2$	624.87	^{18}OOO	625.39	ClO	649.45
CH_3CN	624.88	^{18}OOO	625.56	$(ClO)_2$	649.51
CH_3CN	624.91	O_3 (v_2)	625.61	HO_2	649.70
CH_3CN	624.93	HO_2	625.66	$O^{17}OO$	649.79
$H^{37}Cl$	624.98	OClO	625.78	^{17}OOO	649.97
H_2O_2	625.04	O_3 (v_2)	625.79	^{17}OOO	649.98
O_3 (v_3)	625.05	O_3 (v_3)	625.80	^{17}OOO	650.01
$HO^{35}Cl$	625.07	$O^{17}OO$	625.87	^{17}OOO	650.04
^{18}OOO	625.09	$H^{35}Cl$	625.92	^{17}OOO	650.16
$HO^{81}Br$	625.18	$O^{17}OO$	626.09	^{17}OOO	650.17
O_3 (v_2)	625.28	$O^{17}OO$	626.20	^{81}BrO	650.18
O_3 (v_2+v_3)	625.30	OClO	626.22	HNO_3	650.28
O_3 (v_2)	625.32	$(ClO)_2$	626.32		
$HO^{79}Br$	625.33				
HNO_3	625.34				
O_3	625.37				

values including ones to be measured by the SMILES molecular spectroscopy team.

- Clear atmosphere with no cirrus clouds is assumed.

The simulation has revealed several characteristics of molecular spectra involved in the three frequency bands.

- The ClO spectrum is relatively isolated from other spectra in Band-C.
- The HO_2 spectrum is relatively isolated from other spectra in Band-C.
- The baseline level in the lower sideband is higher than that in the upper sideband, which is due to a strong water vapor transition at 620.701 GHz.
- Band-C is most appropriate among the three bands to observe weak spectra.
- Although the Band-C is not includes normal ozone lines, there is a possibility to acquire some ozone information from the wing emissions of its 650.733 GHz line.
- Two BrO bands are available in the SMILES bands, although the transition around 624.77 GHz in Band-A is superimposed on HNO_3 transitions, and the other around

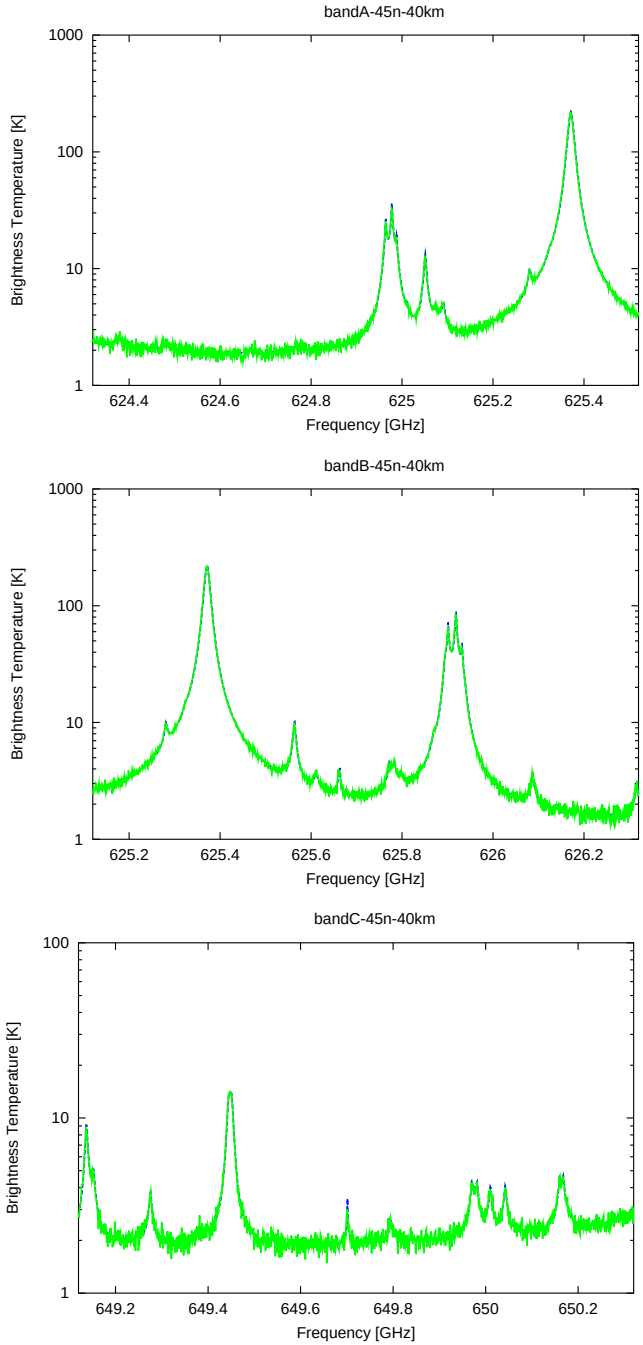

Figure 4.8 SMILES spectra for a tangent height of 40 km simulated with the 45°N model atmosphere. The figures show the quality of observation data accumulated for 30 scans in orbit.

650.18 GHz in Band-C is on isotope ozone transitions. The retrieval error of BrO from the Band-C spectrum is slightly lower than that for the Band-A case.

- Two transitions are available for HO_2, one in Band-B and the other in Band-C. The HO_2 emission in Band-C is relatively isolated from other lines. HO_2 is one of important species with few upper stratospheric and mesospheric data, and it is one

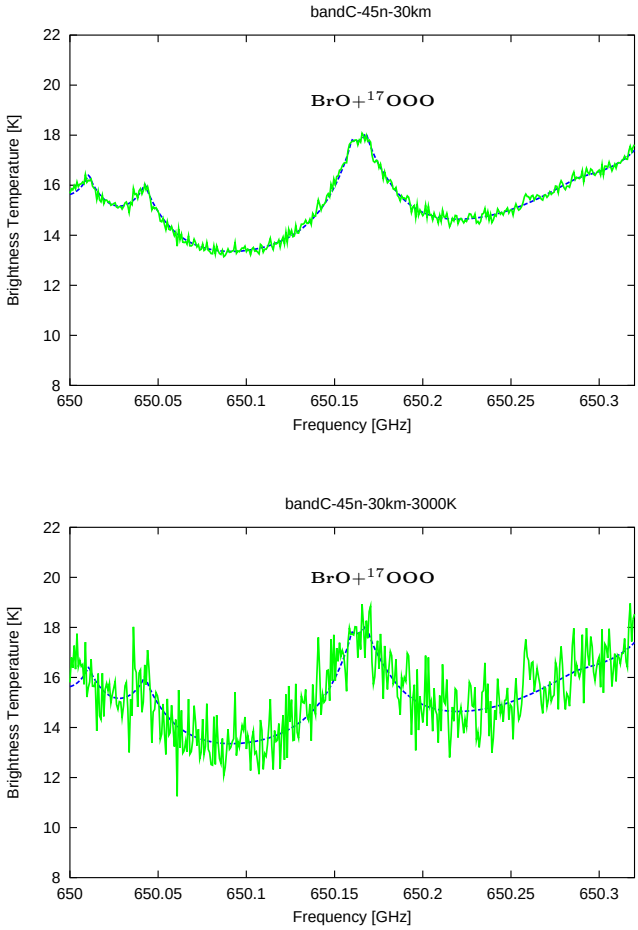

Figure 4.9 Comparison of two spectra, one expected with T_{sys} = 500 K and the other with 3000K.

of surely productive molecules for the SMILES observation.

SMILES's high sensitivity would provide new opportunities to observe stratospheric radical species such as BrO, HO_2 which have been only poorly measured so far. The BrO spectrum that would be obtained by the system with T_{sys} = 500 K (SIS mixer) with accumulations of 30 scans is compared with the same spectrum with 3000 K (Schottky diode mixers) in Figure 4.9.

4.3 Molecular Retrieval

The retrieval of molecular height profiles has been made for SMILES major species by SMOCO, and the outputs are presented in the Appendix. They include the retrieved height profiles, retrieved total errors, and averaging kernels. For the purposes of description, we divide the SMILES species into the next four groups.

- Standard products: O_3, HCl, and ClO in the stratosphere.
- Research products: HOCl, CH_3CN, HO_2, HNO_3, and BrO in the stratosphere.

- Ozone isotopes: asymmetric-18 ozone (^{18}OOO), asymmetric-17 ozone (^{17}OOO), and symmetric-17 ozone (O^{17}OO) in the stratosphere.
- Mesospheric products: O_3, HCl, and HO_2 in the mesosphere.

In the optimal estimation method, the retrieved error informs us how much new observation spectrum with the radiance uncertainty covariance is able to decrease the *a priori* uncertainty covariance, as shown in Equation (4.16). The error ratio, which is defined as the ratio of the total retrieval error to the *a priori* error covariance, is useful to evaluate the retrieval results. We used the error ratio of that sense in the Appendix. The *a priori* error covariance is not a unique value, and different from one species to the other because of its a priori information of the observations, scientific purposes, the intensity of the spectrum in each tangent height, the radiance noise, and so on. For example, in our studies in the Appendix, the diagonal component of *a priori* uncertainty covariance has been assumed to be proportional to the *a priori* height profile in the ratio of 0.5 for the standard products and HNO_3, 1.0 for the research products (except HNO_3), and 0.1 for the ozone isotopes. As the retrieval error thus depends on the *a priori* uncertainty covariance, this value is regarded as an not very good indicator of the measurement capability of an observation system for the purpose of the comparision of each molecular species. To show the instrumental capability directly in this section, the "ERROR" in the figures are presented by the ratio to the *a priori* height profile, instead of the ratio to the *a priori* error.

4.3.1 Standard Products

Three molecular species: O_3, HCl and ClO are classified as the standard products, for which SMILES is expected to give retrieved height profiles with errors less than 10 percent by the use of data available from a single atmospheric scan in orbit. The weighting functions have been calculated with a 2 km step for these species. The "ERROR" are given by their ratios to the retrieved height profiles, which are the same as the *a priori* ones, in Figure 4.11. The *a priori* height profiles used for the retrieval are given in Figure 4.10.

The volume mixing ratio of ClO in the model profile of 80°N enhanced at around 20 km due to the activation of chlorine inside the polar vortex. The single-scan error for this enhanced ClO is estimated less than 10 percent around 20 km. SMILES is also capable of observing ClO in its background abundance that is not enhanced by heterogenious reactions. These are simulated with the atmosphere model height profiles of 45°N. The single-scan error for the case is estimated less than 20 percent for 30 km to 42 km.

With respect to the normal ozone O_3, the retrieval error is estimated less than 5 percent for 20 km to 45 km, and less than 10 percent for 18 km to 52 km at any latitudes even in the case of single scan.

The retrieval error of H^{35}Cl is estimated less than 10 percent for 25 km to 45 km at any latitudes in the case of single scan. It decreases to 5 percent levels for the atmospheric model profiles at 80°N.

4.3.2 Research Products

Five molecular species of HNO_3, HOCl, HO_2, CH_3CN, BrO are classified as the research products, for which SMILES is expected to give retrieved height profiles with errors less than 50 percent by the use of 30-scan averaged data. The weighting functions have been calculated with a 4 km step for these species. The "ERROR" are given by their ratios to the retrieved height profiles, which are the same as the *a priori* ones, in Figure 4.13 and

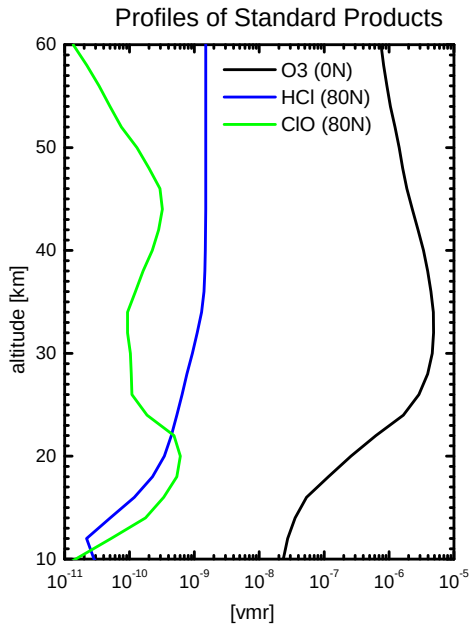

Figure 4.10 The *a priori* molecular height profiles used in the retrieval of the SMILES standard product species. The abscissa is the volume mixing ratio (VMR) of each species.

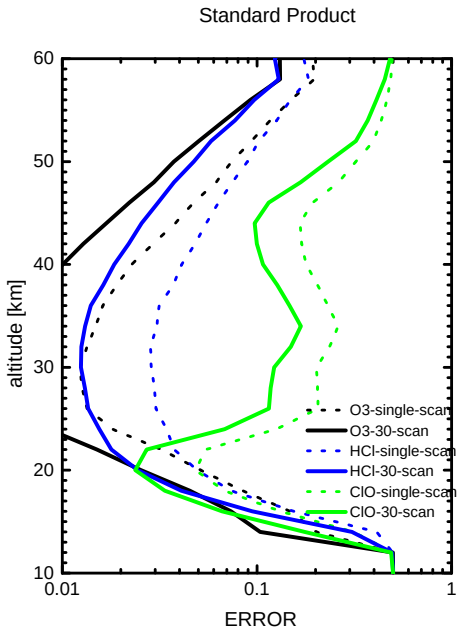

Figure 4.11 The ratio of the retrieval error to the retrieved height profile for the SMILES standard product species.

Figure 4.15. The *a priori* height profiles used for the retrieval are given in Figure 4.12 and Figure 4.14.

With respect to the five research product species, we have retrieved the height profiles from 30-scan averaged data. Among them, HOCl, CH_3CN, and HNO_3 are species that can be retrieved with errors significantly less than 20 percent. The error levels for HOCl are less than 20 percent at any latitudes for 26 km to 43 km. The profiles of CH_3CN are obtained from [*Livesey*, 2001], not model profiles. The error levels for CH_3CN in the equator are less than 20 percent for 15 km to 38 km. HNO_3 is expected to be abundant at high latitudes, and the retrieval errors are less than 20 percent at 17 km to 30 km with the atmospheric model profile at 80°N.

For other two species, i.e., HO_2 and BrO, the error levels are less than 50 percent. Since HO_2 is abundant in the upper stratosphere and mesosphere at low latitude regions, the HO_2 retrieval errors decrease to 30-40 percent levels for higher than 30 km in the equator. The BrO retrieval errors are less than 50 percent at 25 km to 37 km by the atmospheric model profile at 80°N. BrO could be detectable with errors of 50 percent levels even at mid-latitudes profile. Note that we are here talking about the retrieval errors we expect from the 30-scan averaged data, which correspond to a 5-degree latitudinal zonal mean available in half a day. Significant error reduction is therefore very hopeful when we deal with data averaged in much longer periods.

Based on the above investigations, we expect SMILES data will be useful to study the so-called HOx chemistry, including HOCl and HO_2, from aspects of its relations to the ClO chemistry.

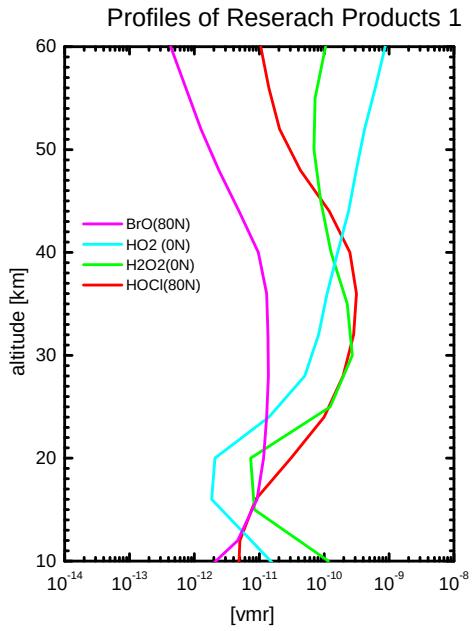

Figure 4.12 The *a priori* molecular height profiles used in the retrieval of the SMILES research product species. The abscissa is the volume mixing ratio (VMR) of each species.

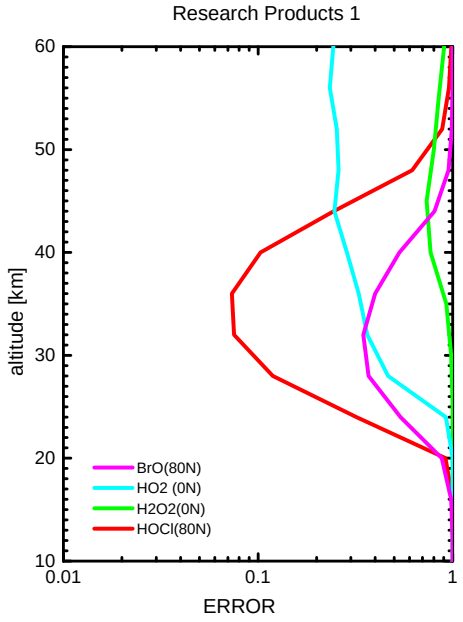

Figure 4.13 The ratio of the total retrieval error to the retrieved height profile for the SMILES research product species.

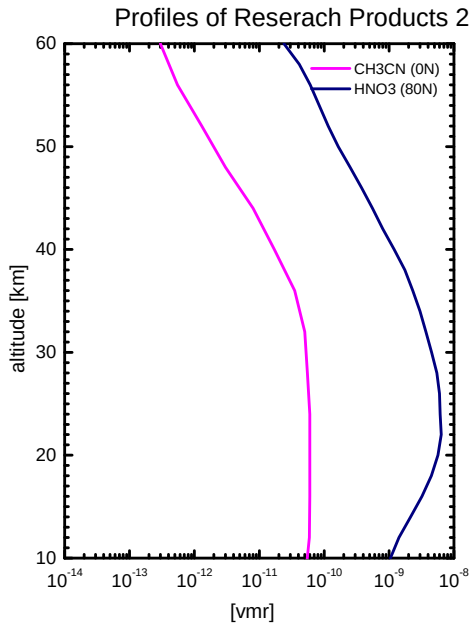

Figure 4.14 The *a priori* molecular height profiles used in the retrieval of the SMILES research product species. The abscissa is the volume mixing ratio (VMR) of each species.

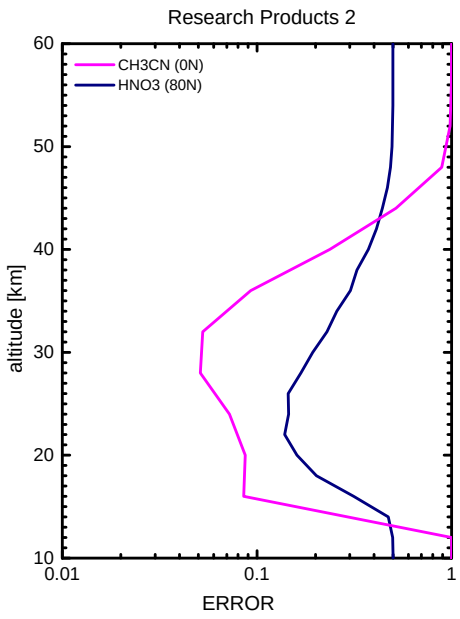

Figure 4.15 The ratio of the total retrieval error to the retrieved height profile for the SMILES research product species.

4.3.3 Ozone Isotopes

There are 73 transitions of ozone isotopes in the three frequency bands of SMILES. Among them, Band-C is most suitable to observe ozone isotopes, since it includes a lot of relatively isolated spectra for asymmetric-17 ozone (^{17}OOO), asymmetric-18 ozone (^{18}OOO), and symmetric-17 ozone (O^{17}OO). The retrieval errors with the 30-scan averaged data are summarized as follows. The "ERROR" are given by their ratios to the retrieved height profiles, which are the same as the *a priori* ones, in Figure 4.17. The *a priori* height profiles used for the retrieval are given in Figure 4.16.

- Normal ozone (O_3): The retrieval errors are less than 2 percent from 21 km to 45 km with a height resolution of 2 km.
- Asymmetric-18 ozone (^{18}OOO): The retrieval errors are less than 2 percent from 24 km to 39 km with a height resolution of 5 km.
- Asymmetric-17 ozone (^{17}OOO): The retrieval errors are less than 2 percent from 25 km to 35 km with a height resolution of 5 km.
- Symmetric-17 ozone (O^{17}OO): The retrieval errors are less than 9 percent from 25 km to 40 km with a height resolution of 5 km.

The retrieved error of isotopes are converted to the error in the isotope enrichment δ. The degree of the ozone isotope enrichment is defined as $\delta^M\mathrm{O} = ({}^M R_{obs}/{}^M R_{std} - 1) \times 1000$ [‰], where ${}^M R_{obs}$ is the observed abundance ratio of the heavy isotopomer with mass

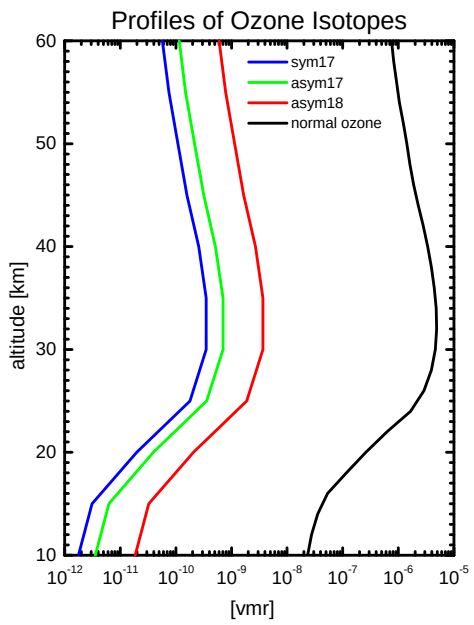

Figure 4.16 The *a priori* molecular height profiles used in the retrieval of the SMILES ozone isotopes. The abscissa is the volume mixing ratio (VMR) of each species.

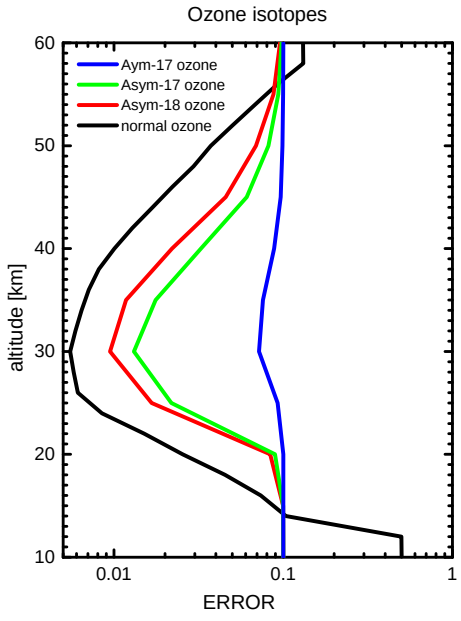

Figure 4.17 The ratio of the retrieval error to the retrieved height profile for the SMILES ozone isotopes.

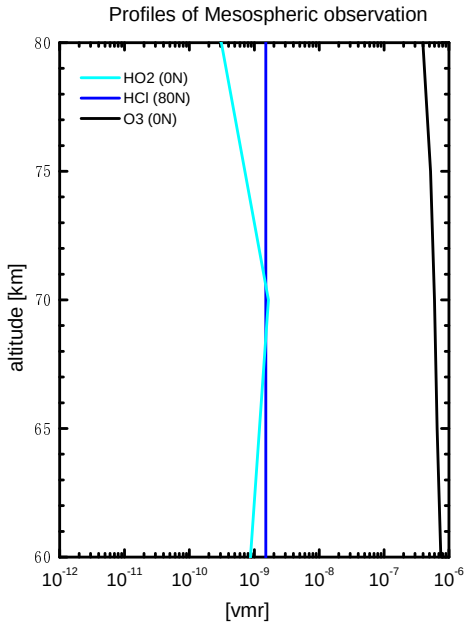

Figure 4.18 The *a priori* molecular height profiles used in the retrieval of the SMILES mesospheric species. The abscissa is the volume mixing ratio (VMR) of each species.

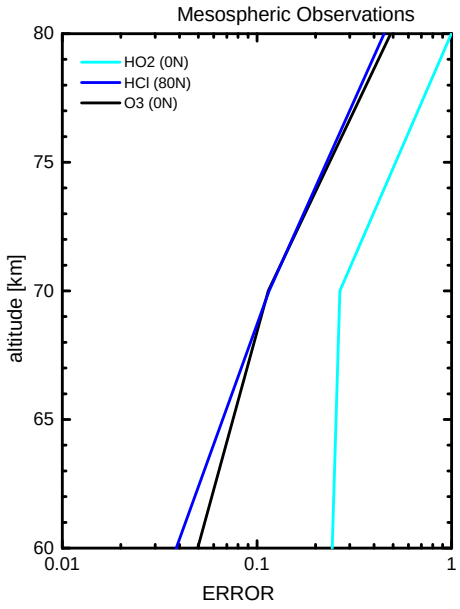

Figure 4.19 The ratio of the total retrieval error to the retrieved height profile for the SMILES mesospheric species.

number M, and ${}^{M}R_{std}$ is the standard ratio described above [*Kaye*, 1987] as described in section 2.4. The error in δ is affected by two retrieval errors: one in the retrieved normal ozone, the other in the retrieved isotope ozone. So it is given by the root-square-sum of the two errors. Since they are estimated as 2 percent for normal ozone and ^{18}OOO, the error in δ for ^{18}OOO is less than 3 percent. The error in δ for ^{17}OOO is also less than 3 percent. The absolute value of δ is expected to be 10–40 % (100–400 ‰) for ^{18}OOO, and around 10 percent (100 ‰) for ^{17}OOO, as described in Chapter 2. Therefore, SMILES will be able to provide useful data for the ozone isotope enrichment. Furthermore, the data will be available in every day and night in 5-degree latitudinal zone maps. SMILES will be the first mission to investigate the global distribution of ozone isotopes.

4.3.4 Mesospheric Products

Among the SMILES spectrum simulation, O_3, HCl and HO_2 are expected to have relative strong line intensity in the mesosphere. We therefore classified these species as the mesospheric products, and conducted the retrieval with a reduced height resolution of 10 km. With the 30-scan averaged data, the retrieval errors are estimated to be less than 50 percent at altitudes of less than 70 km for O_3 and HCl at any latitudes and for HO_2 in the equator model profiles. Although the formal observation range of SMILES is 10-60 km, it will also scan the mesosphere up to around 150 km with an increased speed. If all the spectral data available in the scan period is utilized for the retrieval, then the retrieval errors will be much reduced for the mesosphere. The ERROR are given by their ratios to the retrieved height profiles, which are the same as the *a priori* ones, in Figure 4.19. The

a priori height profiles used for the retrieval are given in Figure 4.18.

4.4 Temperature and Pointing Retrieval

The standard approach for microwave limb sounding instruments is to derive the atmospheric temperature profile and instrumental pointing information from oxygen emission lines [*Wehr*, 1998; *Engeln*, 1998; *Carlotti*, 1999; *Engeln*, 2000]. The oxygen volume mixing ratio is constant and therefore, the intensity of the emission line is only a function of the atmospheric temperature and the total pressure. Nevertheless, other emissions, e.g., ozone emissions, can also convey accurate temperature and pointing information. In that case the information originates primarily from the fact that the limb path becomes opaque for certain tangent altitudes and frequencies. In general, the limb path for the center of the spectral lines becomes opaque at higher tangent altitudes, whereas the limb path for the wings of the spectral lines becomes opaque only at lower tangent altitudes. In the opaque case there is a direct relation between the brightness temperature received by the instrument and the physical temperature of the atmosphere. The width of the spectral line conveys information on the pressure, and thus, information on pointing.

The spectral ranges which will be observed by the SMILES instrument do not include an oxygen emission line and thus information on the atmospheric temperature and instrumental pointing have to be extracted from non-uniformly mixed species emission lines. Therefore it is essential to investigate where the information on the two quantities comes from.

The atmospheric temperature profile and a first order correction of the instrumental pointing, the pointing offset, are retrieved simultaneously with the molecular species profiles. The atmospheric temperature profile is retrieved on a logarithmic pressure vertical grid corresponding to a vertical spacing in altitude of about 3 km. For this, a variance (a priori error) of 5 K was assumed, and no interchannel correlation was considered. The pointing offset is retrieved as an offset in the antenna viewing direction. For this, a standard deviation of 0.2° , corresponding to about 7 km at the tangent point, was considered.

Retrieval simulations were carried out with or without the hydrostatic equilibrium constraint. The full set of presented results refers to mid-latitude summer atmospheric conditions [*Anderson*, 1986].

4.4.1 Temperature Retrieval

4.4.1.1 Information Content

Compared with the molecular species profiles, the derivation of the atmospheric temperature profile is a more complicated process. Information on the atmospheric temperature profile is derived through different mechanisms, as outlined above. To see where the information on the atmospheric temperature comes from the information content in the measurement with respect to the atmospheric temperature is investigated. The information content is given by the $\tilde{\mathsf{K}}$ matrix which is the weighting function matrix K_x scaled by the variability of the a priori state and the measurement [*Rodgers*, 2000]:

$$\tilde{\mathsf{K}} = \mathsf{S}_\epsilon^{-\frac{1}{2}} \mathsf{K}_\mathsf{x} \mathsf{S}_\mathsf{a}^{\frac{1}{2}} \tag{4.31}$$

In the above equation S_ϵ is the measurement noise covariance matrix (in this case a diagonal matrix representing only the thermal noise), and S_a is the a priori covariance matrix (in this case a diagonal matrix with the diagonal elements equal with the variance of the atmospheric temperature profile, i.e., $(5\ \mathrm{K})^2$).

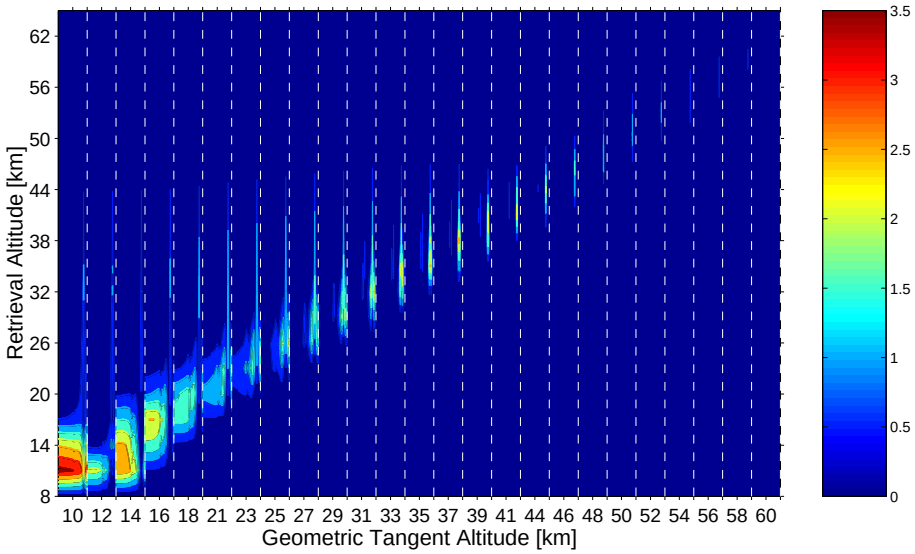

Figure 4.20 Band A: "Information content" on the atmospheric temperature. The x axis displays the measurement vector during one scan. The spectra taken at different tangent altitudes (in the altitude range of 10 – 60 km, in steps of 2.1 km) are separated by vertical dashed lines. The tangent altitudes are displayed at the middle point of the corresponding region of the measurement. The y axis displays the retrieval altitude levels. The retrieval altitudes where there is no information on the temperature (i.e., very low altitudes) are not shown.

As an example, the results for Band A are shown. Figure 4.20 ("Information content") shows the $\tilde{\mathsf{K}}$ matrix for the temperature retrieval in Band A. The x axis displays the measurement vector during one scan (i.e., 25 tangent altitudes, corresponding to altitudes between 10 and 60 km in steps of 2.1 km), while the y axis displays the retrieval altitude levels. The geometric tangent altitudes are placed on the x axis at the middle point of the corresponding part of the measurement. It is seen that the measurement has a high information content with respect to atmospheric temperature at altitudes around 11 km, altitudes where saturation effects occur. At even lower altitudes the atmosphere is totally opaque and thus no information on the temperature can be obtained from the measurement. Similar behavior has been found for the other two bands. In the first two bands, Band A and Band B (not shown), the O_3 transition at 625.37 GHz plays an important role for the temperature profile derivation at higher altitudes. Nevertheless, some information on the temperature comes from spectral features in the frequency ranges around 624.98 GHz (Band A) and 625.92 GHz (Band B), where the HCl emission lines are found. Similar analysis carried out for Band C shows that no information on the temperature is found at higher altitudes, a consequence of the lack of strong spectral features within this spectral band which could provide information on the temperature.

4.4.1.2 With Hydrostatic Equilibrium

The results for the temperature retrieval with hydrostatic equilibrium are displayed in Figures 4.21 – 4.23. The watched quantities are the retrieval precision, the measurement error, the error correlation of the temperature retrieval with the other retrieved quantities, the averaging kernel functions and the vertical resolution given by the full width at half

maximum (FWHM) of the averaging kernel functions.

Figure 4.21(a), Figure 4.22(a) and Figure 4.23(a) show that the atmospheric temperature profile can be retrieved (in all three spectral bands) with a precision better than 1 K at altitudes around 11 km, a consequence of the saturation effects. The first two bands, Band A and Band B, are almost equally suited for the temperature retrieval at most altitudes, a consequence of the fact that the same main source of information, the O_3 line at 625.37 GHz, is used in both bands. The atmospheric temperature profile can be retrieved with a precision of about 1 K up to altitudes of about 40 km in Band A (Figure 4.21(a)), and up to altitude of about 45 km in Band B (Figure 4.22(a)). In this altitude range the retrieval precision is dominated by the measurement error, the smoothing error (not shown) is rather small. The retrieval precision becomes closer to the a priori error at altitudes below 10 km, and above 50 km, a fact which shows that the information on the temperature relies more on the a priori information than on the information from the measurement. The temperature retrieval is somewhat correlated with the HCl retrieval (in Band A also with the HNO_3 retrieval) at low altitudes, and with the O_3 retrieval at high altitudes (Figure 4.21(b) and Figure 4.22(b)). A strong correlation of the temperature retrieval with the pointing offset retrieval is seen at an altitude of 11 km, the altitude where the saturation effects occur, and at 14 km, the reference altitude for the hydrostatic equilibrium. An altitude coverage (i.e., a good measurement response) up to 45 km in Band A (Figure 4.21(c)), and up to 50 km in Band B (Figure 4.22(c)) with a vertical resolution of approximately 3 km (Figure 4.21(d) and Figure 4.22(d)) is achieved. In contrast to the first two bands, the retrieval of the atmospheric temperature profile in Band C is achieved with a much poorer performance (Figure 4.23), a consequence of the fact that in this spectral range there are no strong spectral features which could give information on the atmospheric temperature. Also for this last band, a strong error correlation of the temperature retrieval with the pointing offset retrieval at 11 km (where the saturation effects occur), and at 14 km (the reference altitude for the hydrostatic equilibrium calculation) is seen (Figure 4.23(b)).

4.4.1.3 Without Hydrostatic Equilibrium

The results for the retrieved atmospheric temperature profile without hydrostatic equilibrium are displayed in Figures 4.24 – 4.26. It turns out that the retrieved temperature profile is very little affected by assuming or not assuming hydrostatic equilibrium. A slight improvement in the retrieval precision of the temperature profile at high altitudes is seen for the retrieval scenario without hydrostatic equilibrium. However, the differences are very small. Neither the shape of the averaging kernel functions or the error correlation with other retrieved quantities are changed in a significant way. A slight change in the error correlation is seen with the retrieved pointing offset, a fact which was already expected, as these two quantities are not any longer related through the hydrostatic equation. This change in error correlation is most "visible" in Band B (see for comparison Figure 4.25(b) and Figure 4.22(b)).

It has to be pointed out that the SMILES observation are not done on a vertical line. For each limb scanning, the tangent altitude travels about 100 km in horizontal direction as its altitude increases from 10 km to 60 km. That means that the hydrostatic equilibrium is not fulfilled. However, it is shown that the retrieval performance of the atmospheric temperature profile without hydrostatic equilibrium is comparable – if not better – to one obtained when the hydrostatic equilibrium is assumed.

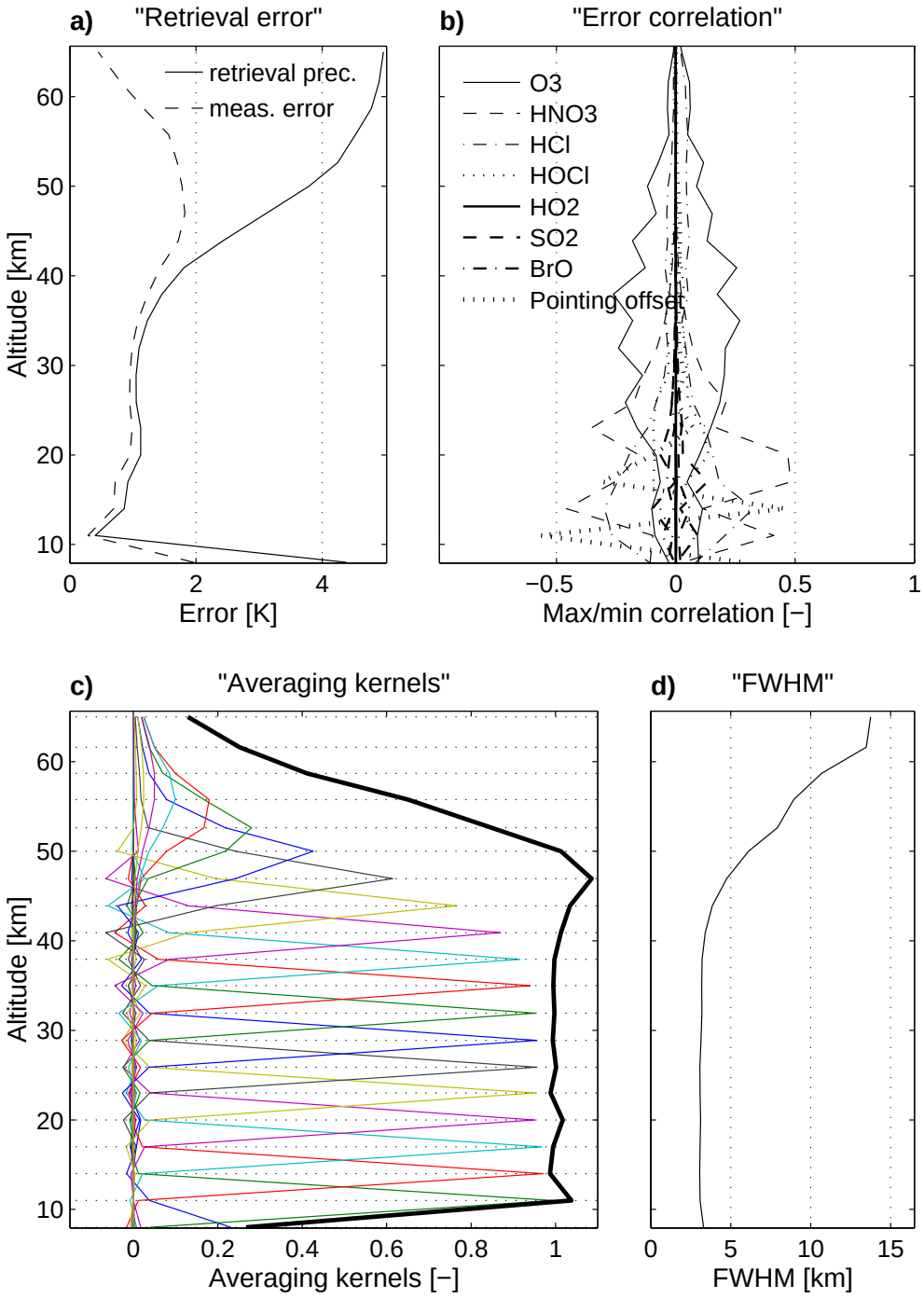

Figure 4.21 Temperature retrieval in Band A with hydrostatic equilibrium: (a) Retrieval precision and measurement error; (b) Error correlation with the other retrieved quantities; (c) Averaging kernel functions; (d) FWHM of the averaging kernel functions presented in (c). The measurement response is also displayed in the plot (c) (solid thick line). Displayed are only those altitudes where a measurement response better than 0.3 is achieved.

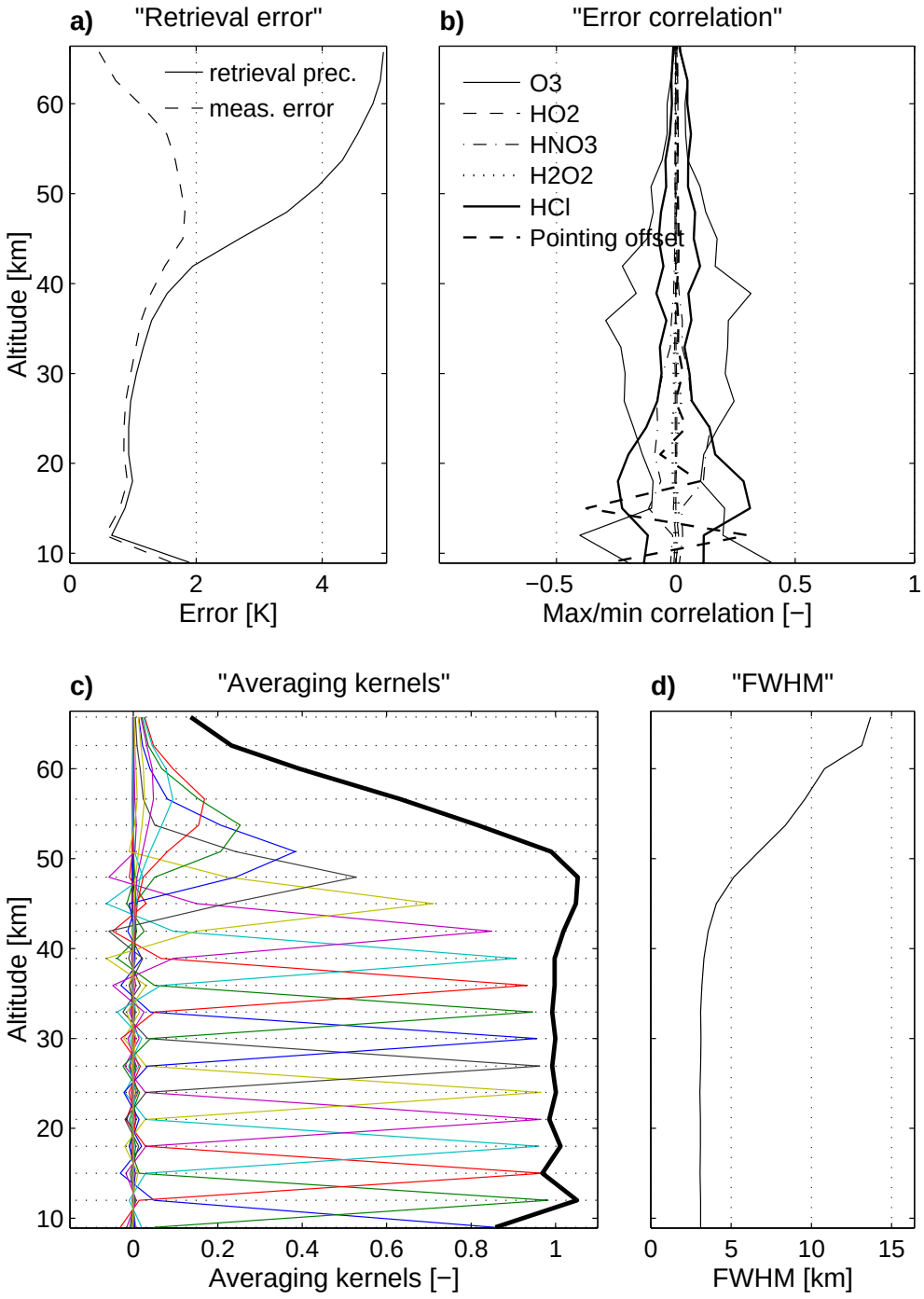

Figure 4.22 Temperature retrieval in Band B with hydrostatic equilibrium: (a) Retrieval precision and measurement error; (b) Error correlation with the other retrieved quantities; (c) Averaging kernel functions; (d) FWHM of the averaging kernel functions presented in (c). The measurement response is also displayed in the plot (c) (solid thick line). Displayed are only those altitudes where a measurement response better than 0.3 is achieved.

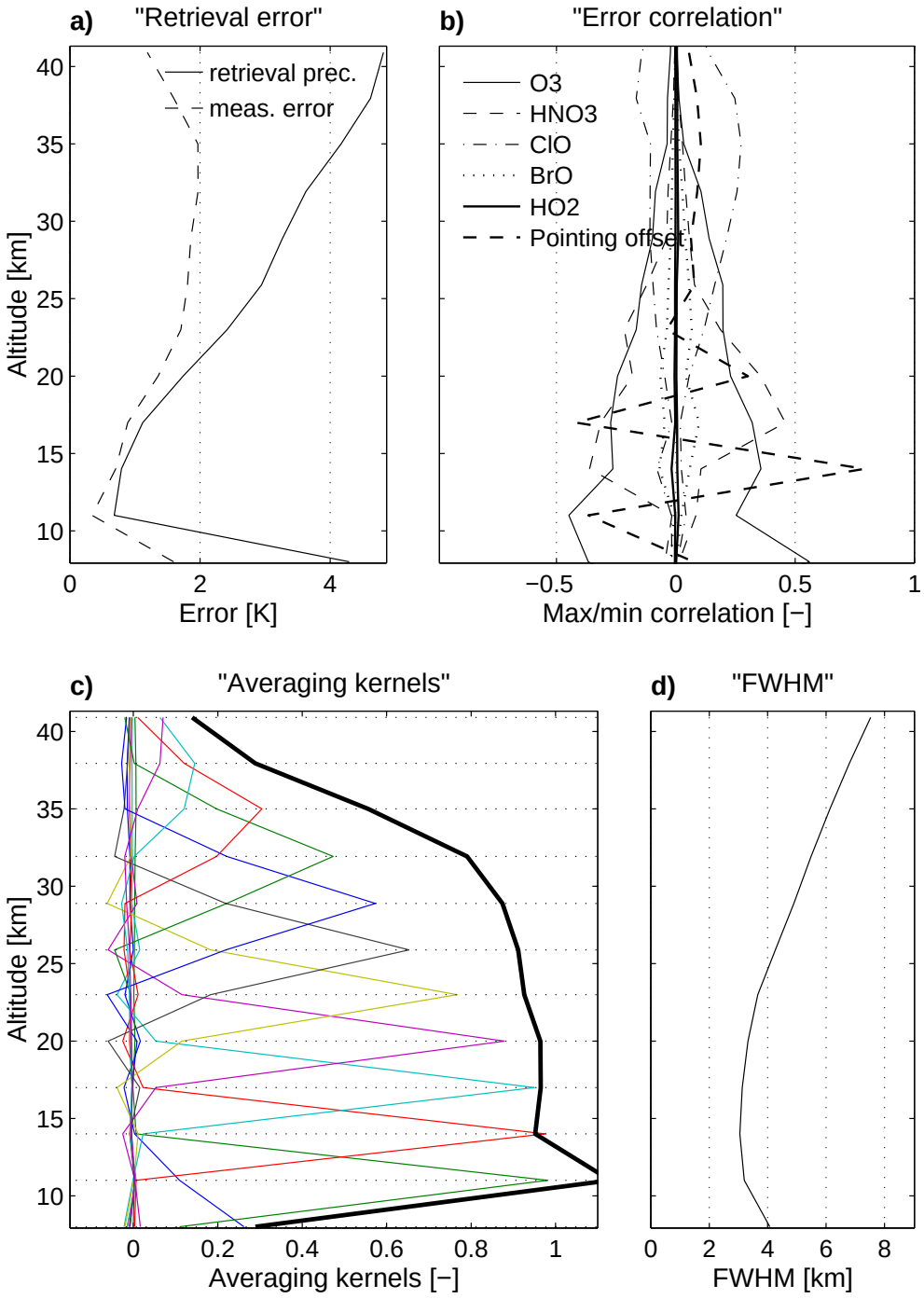

Figure 4.23 Temperature retrieval in Band C with hydrostatic equilibrium: (a) Retrieval precision and measurement error; (b) Error correlation with the other retrieved quantities; (c) Averaging kernel functions; (d) FWHM of the averaging kernel functions presented in (c). The measurement response is also displayed in the plot (c) (solid thick line). Displayed are only those altitudes where a measurement response better than 0.3 is achieved.

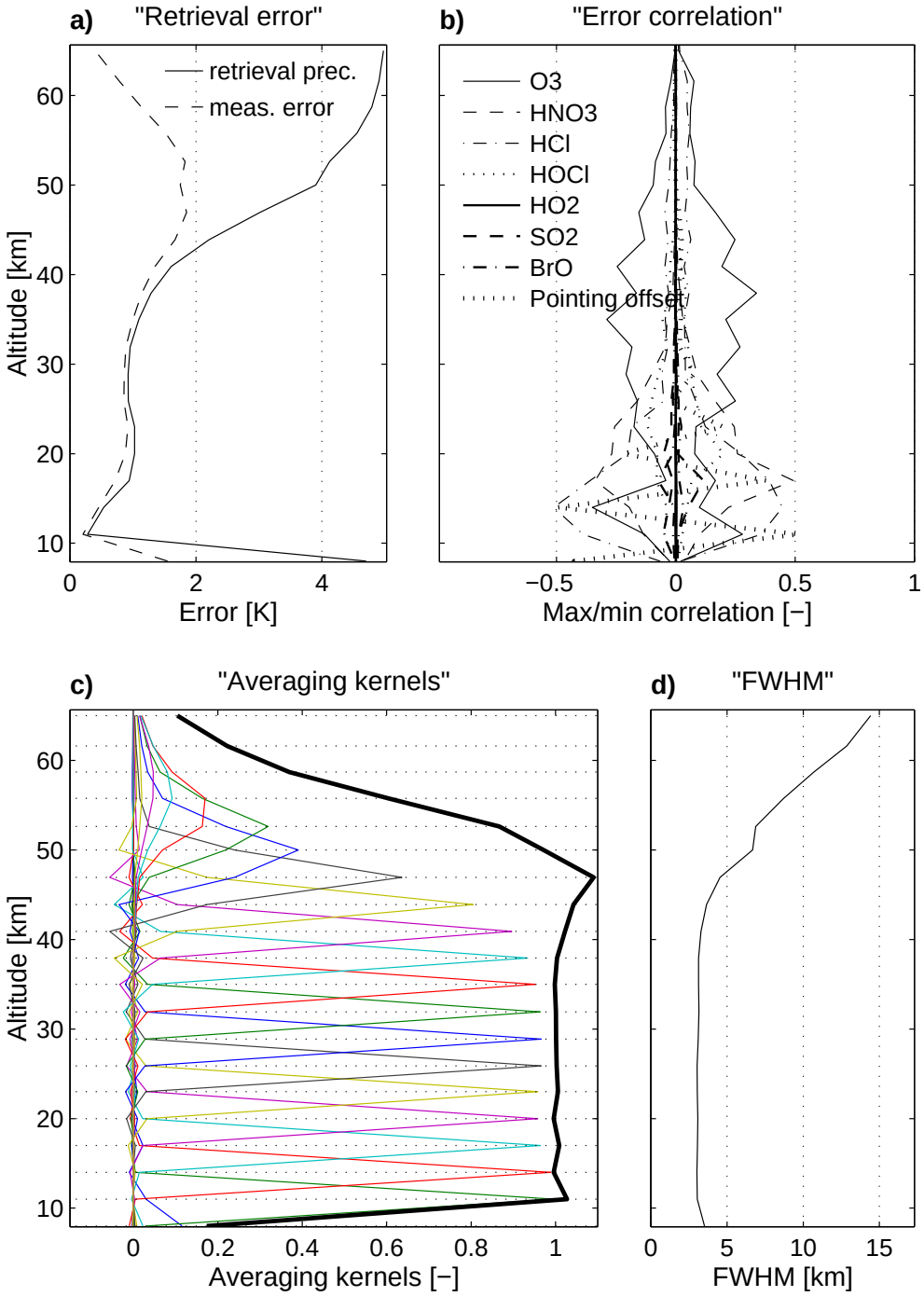

Figure 4.24 Temperature retrieval in Band A without hydrostatic equilibrium: (a) Retrieval precision and measurement error; (b) Error correlation with the other retrieved quantities; (c) Averaging kernel functions; (d) FWHM of the averaging kernel functions presented in (c). The measurement response is also displayed in the plot (c) (solid thick line). Displayed are only those altitudes where a measurement response better than 0.3 is achieved.

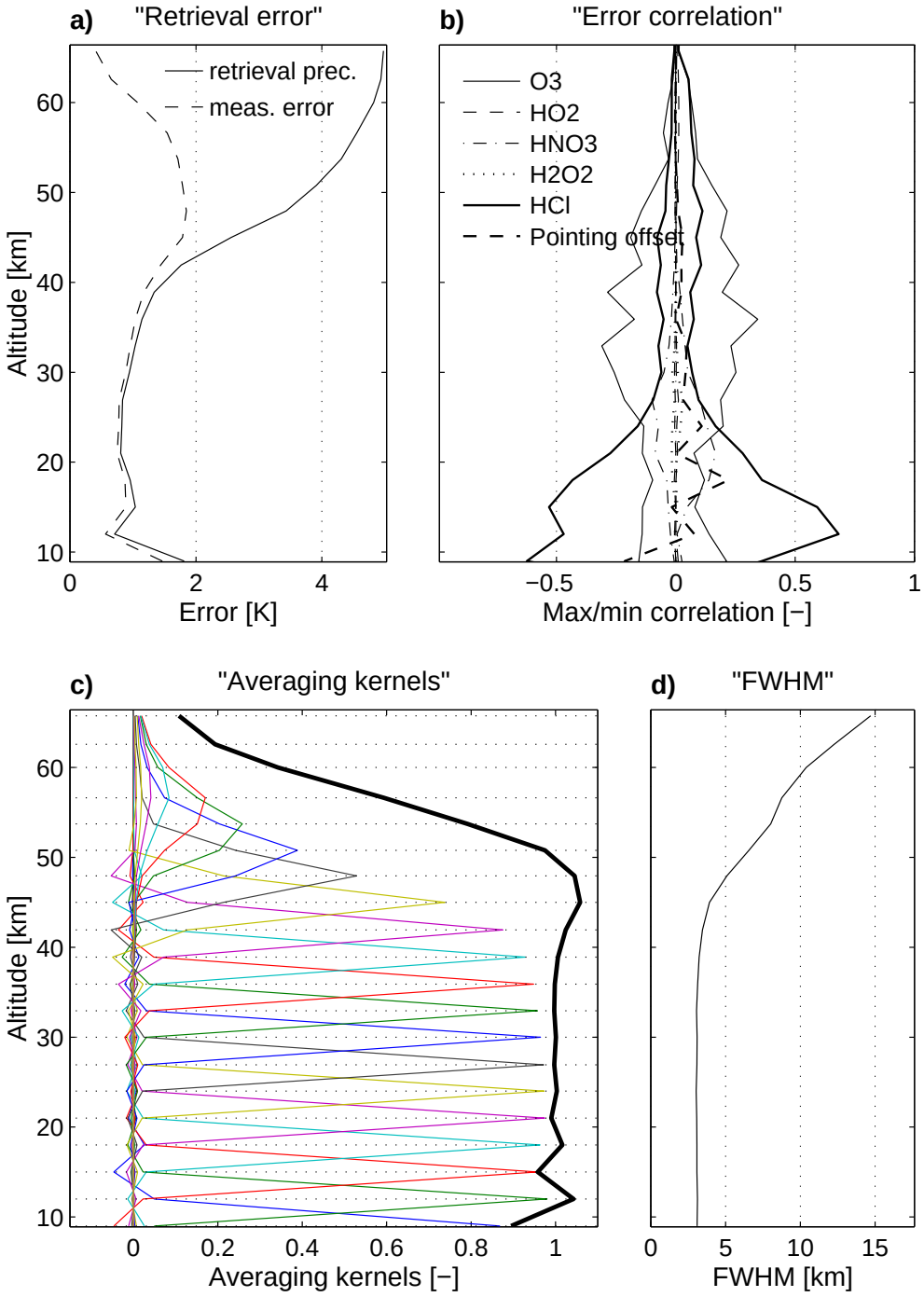

Figure 4.25 Temperature retrieval in Band B without hydrostatic equilibrium: (a) Retrieval precision and measurement error; (b) Error correlation with the other retrieved quantities; (c) Averaging kernel functions; (d) FWHM of the averaging kernel functions presented in (c). The measurement response is also displayed in the plot (c) (solid thick line). Displayed are only those altitudes where a measurement response better than 0.3 is achieved.

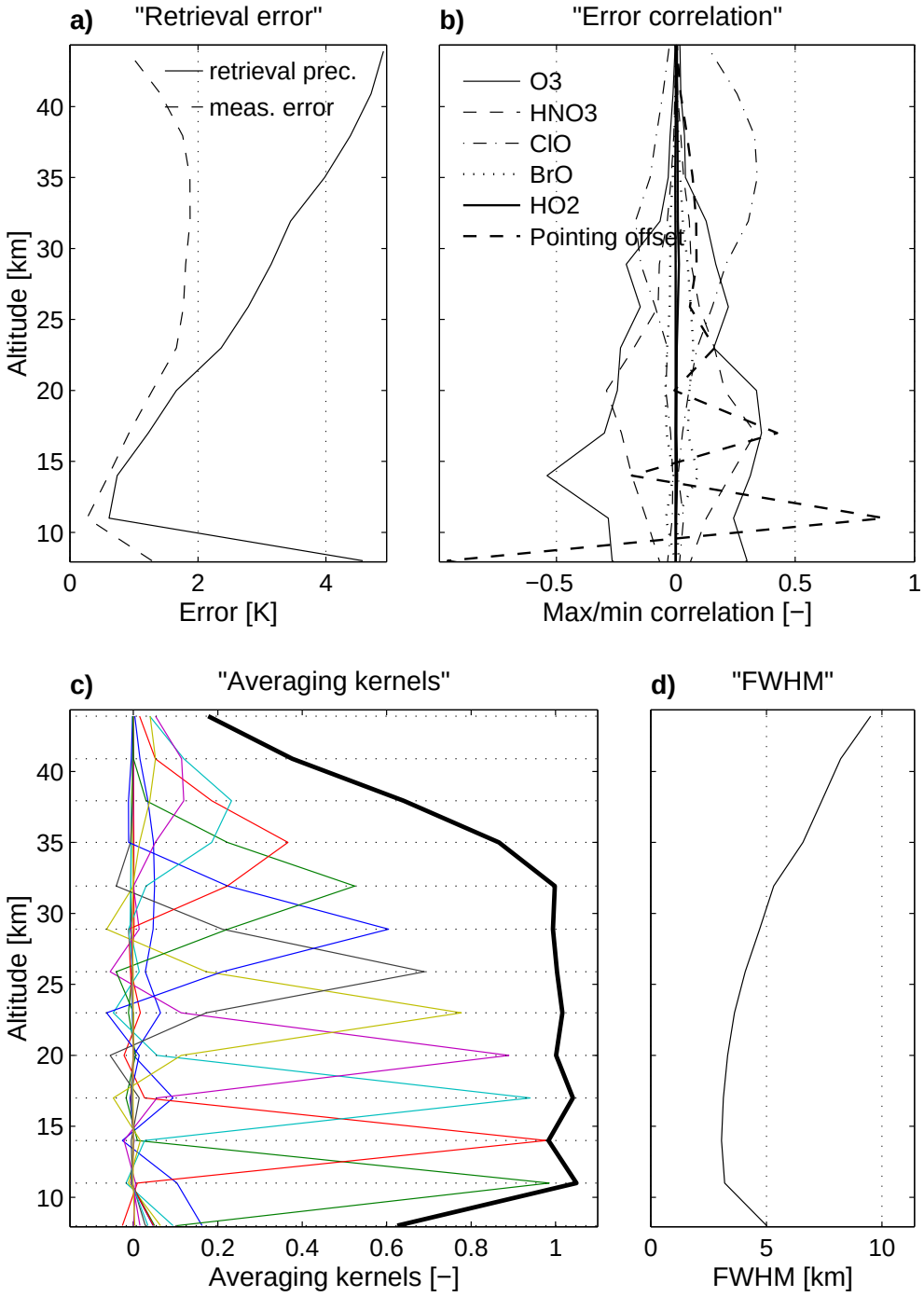

Figure 4.26 Temperature retrieval in Band C without hydrostatic equilibrium: (a) Retrieval precision and measurement error; (b) Error correlation with the other retrieved quantities; (c) Averaging kernel functions; (d) FWHM of the averaging kernel functions presented in (c). The measurement response is also displayed in the plot (c) (solid thick line). Displayed are only those altitudes where a measurement response better than 0.3 is achieved.

4.4.2 Pointing Offset Retrieval

The same steps as for the temperature retrieval were done for the pointing offset retrieval. That means that the information content in the measurement of the pointing offset is analyzed, and the retrieval performance is investigated with or without hydrostatic equilibrium constraint.

4.4.2.1 Information Content

Since no analytical expression is known to calculate the weighting function for the pointing offset, this has to be calculated numerically. The most general and also the most straightforward way to calculate the weighting function is by doing disturbance calculations by repeated use of the forward model. For example, the weighting function for the i^{th} component of the state vector can be calculated by:

$$K_{\mathsf{x_i}} = \frac{\mathbf{F}(\mathsf{x_a} + \Delta\mathsf{x_i}\mathsf{i_i}, \mathsf{b_a}) - \mathbf{F}(\mathsf{x_a}, \mathsf{b_a})}{\Delta\mathsf{x_i}} \tag{4.32}$$

where $\Delta\mathsf{x_i}$ is a small disturbance of the i^{th} component of the state vector (in this case pointing offset), and $\mathsf{i_i}$ is a vector of zeros except the i^{th} component that is unity. The weighting function of the pointing offset reflects the change of the emission for a small change in viewing angle. The magnitude of the disturbance $\Delta\mathsf{x_i}$ plays an important role. Theoretically, the smaller $\Delta\mathsf{x_i}$, the more accurate the result. However, the value applied practically must not be too small as this could lead to numerical instabilities. The value applied here to calculate the weighting function of the pointing offset is 0.001°, found to be small enough the get acceptable results. The information content of the measurement on the pointing offset is given by $\tilde{\mathsf{K}}$ (Equation 4.31). As the pointing offset is described by a single variable, the weighting function matrix has only one column, and so has the $\tilde{\mathsf{K}}$ matrix therefore.

Figure 4.27 displays the $\tilde{\mathsf{K}}$ matrix for the pointing offset, in the three SMILES bands. The presented results refer to the retrieval scenario with hydrostatic equilibrium constraint. However, retrieval simulations carried out without hydrostatic equilibrium constraint showed similar results. The $\tilde{\mathsf{K}}$ matrix is displayed for the measurement taken during one scan. The tangent altitude for each spectrum is displayed in the middle point of the corresponding region of the measurement vector.

The emission at upper tropospheric and lower stratospheric altitudes is dominated by the continuum absorption from O_2, N_2, and H_2O, but also from the line wings of the O_3 emission. Therefore the measurement is characterized by a rather flat, with respect to frequency, information content on the pointing offset. At even lower tangent altitudes the atmosphere is optically thick and the emission is fairly constant explaining the rapid decrease of the measurement information content on the pointing offset at altitudes between 9 and 12 km. These features appear in all there bands. For Band A and Band B, the optical thickness is especially high around the center frequency of the O_3 transition at 625.37 GHz (Figure 4.27, top and middle plots) and so no information on the pointing offset is obtained at this frequency. At higher altitudes the information comes mainly from the O_3 line wings. The features of the HCl lines at 624.98 GHz (Band A) and 625.92 GHz (Band B) show weakly up at high altitudes. Looking at Figure 4.27 it can be concluded that the best altitudes to derive information on the pointing offset in the spectral ranges of Band A and Band B are between 12 and 18 km, due to the continua and O_3 absorption, and between 30 and 50 km where the information on the pointing offset is mainly gained from the wings of the O_3 emission line. From these figures one can clearly see that the pressure broadening linewidth plays an important role in deriving information

on the pointing offset; the shape of the "Information content" curve for different tangent altitudes changes according to the width of the O_3 emission line. In case of Band C the information on the pointing offset is obtained only at low altitudes, due to the continuum absorption (Figure 4.27, bottom plot). For this band, the best altitudes to retrieve the pointing offset are found between 12 and 16 km.

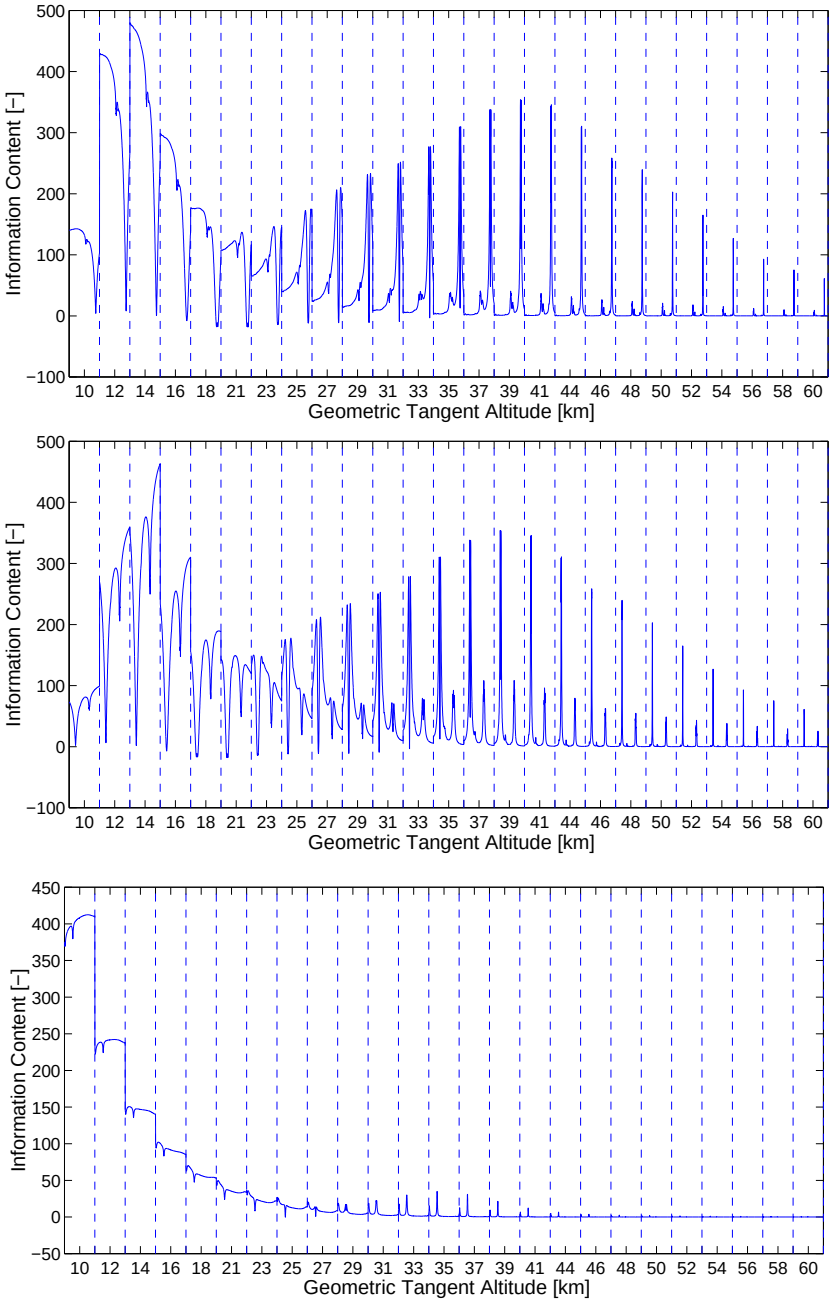

Figure 4.27 "Information content" of the measurement on the pointing offset. Top: Band A; Middle: Band B; Bottom: Band C. The x axes display the measurement vector during one scan (i.e., 25 tangent altitudes), while the y axes display the retrieval altitude levels. The geometric tangent altitudes are placed at the middle point of the corresponding part of the measurement (on the x axes). The presented calculations have been performed under the constraint of the hydrostatic equilibrium.

Table 4.3 Retrieval precision, measurement error and measurement response for the retrieved pointing offset. The retrieval precision and measurement error are given both in antenna viewing angle units [degree] and in the tangent altitude units [m]. The results refer to the retrieval scenario with hydrostatic equilibrium and for the atmospheric conditions specific to mid-latitude summer.

Term		Band A	Band B	Band C
retrieval precision	absolute [°]	$9.12\ 10^{-5}$	$9.60\ 10^{-5}$	$2.91\ 10^{-4}$
	absolute [m]	4	4	11
measurement error	absolute [°]	$7.03\ 10^{-5}$	$8.78\ 10^{-5}$	$2.72\ 10^{-4}$
	absolute [m]	3	3	10
measurement response		1	1	1

4.4.2.2 With Hydrostatic Equilibrium

Table 4.3 displays the results for the pointing offset retrieval with hydrostatic equilibrium. Listed are the retrieval precision and the measurement error (given both in antenna angle units [degrees] and in tangent altitude units [m]) and the measurement response. The pointing offset can be retrieved with an extremely good precision in all three spectral bands. A perfect measurement response is achieved in all three bands. The first two bands, Band A and Band B, are almost equally well suited for the pointing offset retrieval. This is achieved with a precision of about 0.0001° in the antenna viewing angle, corresponding to a value of few meters in the tangent altitude. For these two bands the retrieval precision is mainly dominated by the measurement error (Table 4.3). The results obtained for Band C are slightly poorer.

Generally, the pointing offset retrieval was found to be highly correlated with the temperature retrieval, and slightly weaker correlated with the O_3 retrieval. In case of Band A and Band B a correlation of the pointing offset retrieval with the HCl retrieval was also found.

4.4.2.3 Without Hydrostatic Equilibrium

Similar results for the pointing offset retrieval without hydrostatic equilibrium are given in Tables 4.4. The same as for the temperature retrieval, the results are slightly influenced by assuming or not assuming the hydrostatic equilibrium. Within one band, the pointing offset is retrieved with a similar precision for the two retrieval scenarios. Only the level of error correlation of the retrieved pointing offset with the other retrieved quantities is slightly changed. This mainly refers to the error correlations with the temperature retrieval, a fact which was already expected as the two quantities are not any longer connected through the hydrostatic equilibrium.

Table 4.4 Retrieval precision, measurement error and measurement response for the retrieved pointing offset. The retrieval precision and measurement error are given both in antenna viewing angle units [degree] and in the tangent altitude units [m]. The results refer to the retrieval scenario without hydrostatic equilibrium and for the atmospheric conditions specific to mid-latitude summer.

Term		Band A	Band B	Band C
retrieval precision	absolute [°]	$8.96\ 10^{-5}$	$1.09\ 10^{-4}$	$2.38\ 10^{-4}$
	absolute [m]	3	4	9
measurement error	absolute [°]	$7.08\ 10^{-4}$	$1.02\ 10^{-4}$	$2.82\ 10^{-4}$
	absolute [m]	2	3	3
measurement response		1	1	1

4.5 Spectroscopic Data for SMILES

4.5.1 Spectroscopic Data Required for the JEM/SMILES Experiment

The identification and monitoring of atmospheric molecules as well as interstellar molecules critically depend on the laboratory measurements of line positions, intensities, and collisional cross sections (pressure broadening parameters). The transition frequencies that fall into the submillimeter-wave region which the JEM/SMILES aims at have mostly not been directly measured. Majority of them have been extrapolated from the values measured in the lower frequency regions. As a result, it is not surprising to find discrepancies of several MHz, sometimes much larger, between the calculated and measured transition frequencies. Moreover, crucial parameters other than the center frequencies such as the pressure broadening parameters and the pressure line shifts have been, in many cases, unknown. In particular, information for minor constituents like free radicals and very reactive species are extremely incomplete, and the detection of these species themselves constitutes a great challenge for the laboratory spectroscopy.

Therefore a tremendous amount of efforts has been made to create a number of spectroscopic databases: ATMOS [*Brown et al.*, 1987], SAO [*Chance et al.*, 1994], GEISA [*Husson et al.*, 1992; *Husson et al.*, 1994], JPL [*Poynter and Pickett*, 1985; *Pickett et al.*, http://spec.jpl.nasa.gov/], HITRAN [*Rothman et al.*, 1987; *Rothman et al.*, 1992; *Rothman et al.*, 1996]. More recently the Cologne Database for Molecular Spectroscopy (CDMS) is a new addition [*Müller et al.*, http://www.ph1.uni-koeln.de/vorhersagen/]. The JPL catalog [*Poynter and Pickett*, 1985] includes line positions and line intensity parameters. Line broadening and line shift parameters are not listed in this database. Molecules that are of great importance in the JEM/SMILES mission are listed in Table 4.2. The values for these minor constituents listed in the known database may not be accurate enough. A molecular spectroscopy group has been organized to provide and to evaluate important molecular parameters, especially pressure broadening parameters for the JEM/SMILES mission. The measurements have mostly taken place at Ibaraki University.

Among the transitions listed in Table 4.2, O_3, HO_2, HOCl, HNO_3 (except for $29_{25,4} - 28_{25,3}$), other minor isotopic species, and the vibrationally excited states have not been measured. A most urgent task of the laboratory spectroscopy is to confirm and/or improve the transition frequencies and the pressure broadening parameters of the target molecules,

including common molecules such as O_3 and HCl. In particular, systematic discrepancies are often noticed among the pressure broadening parameters obtained at different locations. In this respect, it is almost imperative to check the parameters that are thought to be well established. One of the goals set by the JEM/SMILES mission is to obtain a global map of BrO. To derive reliable quantitative map by inverting the observed line features, the pressure broadening parameters accurate to a few percent are indispensable for the BrO transitions. These crucial parameters for the SMILES target molecules, BrO, HO_2, and, O_3, are now being measured by the molecular spectroscopy team.

4.5.2 Laboratory Submillimeter-wave Spectrometer System

A submillimeter-wave spectrometer system of a wide frequency coverage and high-sensitivity has been implemented. Figure 4.28 shows a schematic diagram of a system at Ibaraki University. Characteristic features of this instrument are: (1)use of backward-wave oscillators manufactured by a Russian company(ISTOK) as radiation sources and (2) double modulation detection scheme, whenever it is applicable. An oscillator tube(BWO) is housed between the pole faces of a permanent magnet of about 1 T of field strength. The free running frequency fluctuation of BWOs reaches over 10 MHz and therefore active frequency stabilization is essential for high-sensitivity and high-resolution spectroscopy. We achieved this goal by using a double phase-lock loop: the submillimeter-wave radiation is phase-locked to a harmonics of millimeter-wave radiation from a stabilized Gunn oscillator by means of a GaAs harmonic mixer fabricated in G. Winnewisser's group at Universität zu

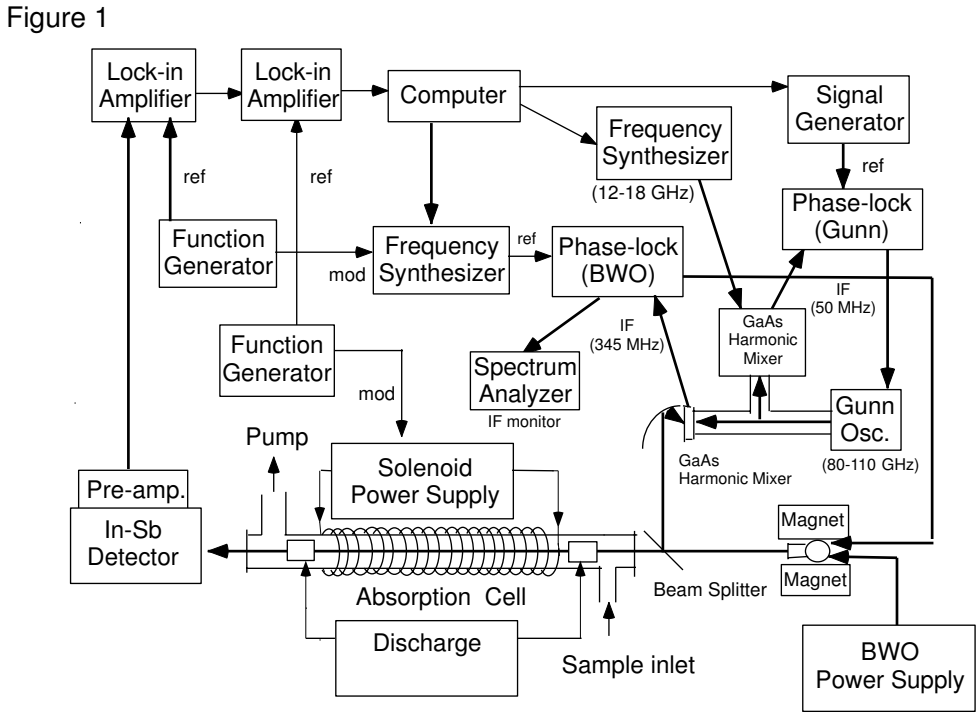

Figure 4.28 A schematic diagram of a double modulation submillimeter-wave system at Ibaraki University.

Köln. The Gunn frequency is stabilized to a harmonics of the microwave frequency(12-18 GHz) generated by a microwave synthesizer.

The submillimeter-wave output is focused by a Teflon lens to make it a parallel beam to direct through the absorption cell. A part of the power is directed to a GaAs mixer by a wire grid beam splitter. The frequency region of 380-850 GHz can be covered with three BWOs. The output power is typically a few milliwatts but it varies greatly over its frequency range. The spectrometer functions very well to the level that we initially aimed at. The submillimeter-wave lines of HO_2 was systematically measured in the range of 400-680GHz. Although the majority of transition frequencies listed in the JPL Catalog agree reasonably well with our measurements, several cases of uncomfortable discrepancy were encountered.

4.5.3 Available Molecular Parameters up to Present

Table 4.5 shows the pressure broadening parameters, γ_0, and its temperature exponent, n, defined as $\gamma(\mathrm{T}) = \gamma_0 \times (\frac{\mathrm{T}}{\mathrm{T}_0})^n$. An example of the line profile of BrO is shown in Figure 4.29. It is almost impossible to fit each hyperfine component separately to a Voigt line profile. To alleviate this difficulty a convolution method proposed by Pickett has been adopted. The pressure broadening parameters thus determined are indicated in the table in boldface. The JPL group has also been performed similar measurements. Their results are compared also in the table. The spectroscopy group of Sciences and Technologies University of Lille has recently reported the pressure broadening parameters of submillimeter-wave transitions of O_3 and BrO. We included their values also in the table. Other parameters in the table were taken from original papers, Aura reports, or HITRAN database. These values should be critically evaluated.

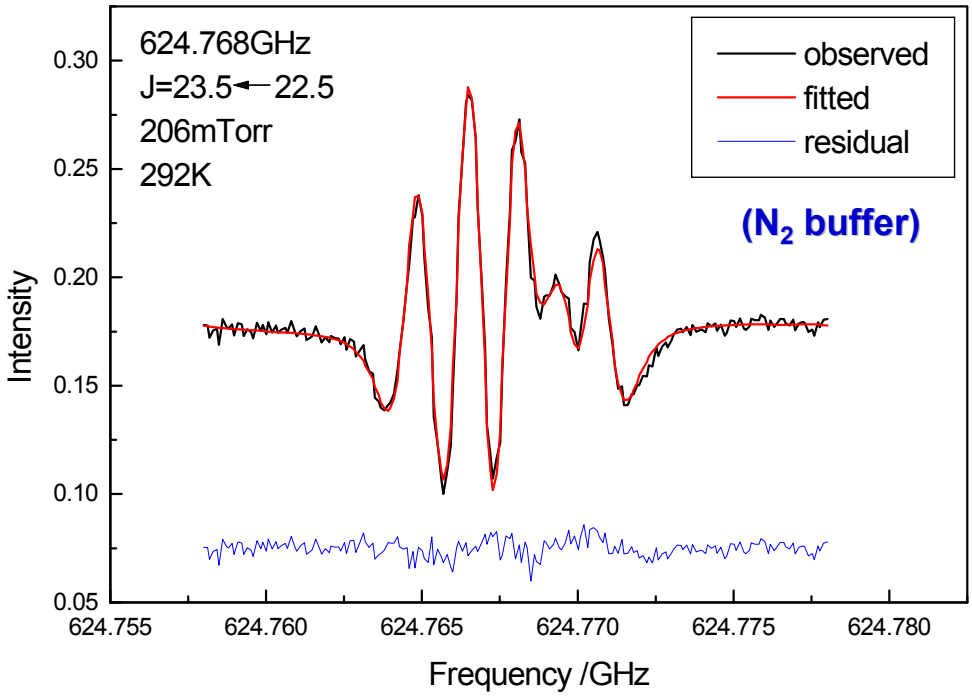

Figure 4.29 A least square fitting of the BrO spectrum to derive the pressure broadening parameter

Table 4.5 Pressure broadening parameters

molecule	frequency [GHz]	γ_0 [MHz/Torr]	n (T_0=294 K)	reference
HNO_3	181.5496	4.362	0.75	1
	369.258	4.16	0.70	2
	624.48	4.339	0.75	3
	624.78	4.339	0.75	3
	650.28	4.339	0.75	3
CH_3CN	624.8			
^{79}BrO	499.6	3.54(28)	0.45(18)	4
^{81}BrO	624.768	**3.01 (10)**		5
	624.768	3.11 (16)	0.66(3)	9
	650.179	**3.03 (10)**		5
	650.179	3.03 (15)	0.56(3)	9
$H^{37}Cl$	624.98	3.51	0.69	3
$H^{35}Cl$	625.9188	3.48	0.74	1
H_2O_2	625.04	3.944	0.50	3
	IR	3.94		6
$HO^{35}Cl$	625.075	2.37	0.5	7
HO_2	641.643	3.16	0.67	3
	641.643	**3.70 (5)**		5
	649.702	**3.37 (11)**		5
	649.702	3.71 (22)	0.2	9
ClO	649.4512	2.81(8)	0.85(9)	8
O_3	206.1320	2.890	0.75	1
	498.7	2.859(11)	0.740(24)	4
	500.4	2.798(57)	0.876(80)	4
	501.8	2.785(28)	0.784(62)	4
^{18}OOO	625.370	2.789	0.76	3
	650.011	2.777	0.76	3

[1]Aura report
[2]T. Goyette, W. Guo, F.C.Delucia, and P. Helminger,
J. Quant. Spectrosc. Radiat. Transfer **46**, 293 (1991)
[3]Hitran 96 database
[4]M. Birk, G. Wagner *et al. Study on a spectroscopic database for millimeter and submillimeter wavelength*, Final report
[5]This work, measured by M. Yamada, M. Kobayashi, H. Habara,
and T. Amano at Ibaraki Univ.
[6]V. Malathy Devi, C.P.Rinsland, M.A.H.Smith, D.Ch.Benner,
and B.Fridovitch, Appl. Opt. **25**, 1844 (1986)
[7]HITRAN default value
[8]J.J.Oh and E.A.Cohen, J. Quant. Spectrosc. Radiat. Transfer **52**, 151 (1994)
[9]E.A.Cohen et al. preliminary results, private communication

4.5.4 Plans for Further Improvement of Data

Preliminary results of the temperature dependence of the pressure broadening parameters for BrO and HO_2 molecules have been obtained. Monitoring the atmospheric abundances

of the minor isotopic species of O_3 is a major scientific objective of the SMILES mission. However, spectroscopic data of the minor isotopic species of O_3 are sparse. Therefore, systematic measurements of these species should be undertaken. The pressure broadening parameters for HCl and HOCl also seems unsatisfactory. The pressure broadening parameters are prone to systematic errors. Coordinated arrangements to critically check data obtained at different institutions are highly desirable.

A remaining problem is to experimentally establish the transition intensity. To derive the precise intensity, the dipole moment should be known. A most commonly used and best established method to obtain dipole moments is Stark effect measurements. For stable molecules such as O_3 and HCl, the dipole moments are obtained precisely. However, it is not always the case for unstable molecules. The dipole moments for HO_2 and BrO are known for quite some time. It is, however, imperative to check them again, because those Stark effect measurements had been performed at a rather early stage of microwave spectroscopy and have not been checked ever since.

References

Anderson, G. P., and S. A. Clough and F. X.Kneizys, and E. P. Shettle, AFGL atmospheric constituents (1-120 km), *Tech. Rep., Nr. TR-86-0110*, 1986.

Brown, L. R., C. B. Framer, C. P. Rinsl, and R. A. Toth., Molecular line parameters for the atmospheric molecule trace spectroscopy experiment, *Appl. Optics, 26*,5154, 1987.

Bühler, S., A. von Engeln, and K. Künzi and B.-M. Sinnhuber, J. Urban, R. Siddans, B. J. Kerridge, W. J. Reburn, R. Peter and K. Arzner The Retrieval of Data from Sub–Millimeter Limb Sounding, Final Report, *Contract No 11979/97/NL/CN*, Noordwijk, February, 1999.

Carlotti, M., B. Carli and M. Ridolfi, Derivation of temperature and pressure from submillimetric limb observations, *ESTEC, Contract No 10306/93/NL/CN*, Final Report, December, 1994.

Chance, K., K. W. Juckes, D. G. Johnson, and W. A. Traub. The Smithsonian Astrophysical Observatory Database SAO92, *J. Quant. Spectrosc. Radia. Transfer, 52*, 447, 1994.

Chandrasekhar, S., *Radiative transfer*, Dover Publications Inc., 393p, New York, 1960.

von Engeln, A., S. Bühler, J. Langen, T. Wehr, and K. Künzi, Retrieval of upper stratospheric and mesospheric temperature profiles from Millimeter-Wave Atmospheric Sounder data, *J. Geophys. Res.*, Volume *103*, pp. 31735-31748, 1998.

von Engeln, A., Satellite based Temperature Profile Determination using Microwave and Radio Occultation Instruments, *PhD. Thesis*, University of Bremen, Germany, Logos Verlag Berlin, 2000, ISBN 3-89722-453-4, ISSN 1615-6862.

Eriksson, P., F. Merino, D. Murtagh, P. Baron, and P. Richau and d. l. Noe, Studies for the Odin sub-millimetre radiometer: 1. Radiative transfer and instrument simulation, To appear in *Canadian Journal of Physics*, 2001.

Husson, N., B. Bonnet, N. A. Scott, and A. Chedin. Management and study of spectroscopic information: GEISA peogram, *J. Quant. Spectrosc. Radia. Transfer, 48*, 509, 1992.

Husson, N., B. Bonnet, N. A. Scott, A. Chedin, A. A. Churisn, V. F. Golovko, and V. G. Tyuterev. The GEISA data bank in 1993: A PC/AT compatible computers' new version, *J. Quant. Spectrosc. Radia. Transfer, 52*, 425, 1994.

Liebe, H. J, MPM - An atmospheric millimeter-wave propagation model. *Int. J. Infrared Millimeter Waves, 10*, 631-650, 1989.

Liebe, H. J, G.A.Hufford, and M.G.Cotton, Propagation modeling of moist air and suspended water/ice particles at frequencies below 1000 GHz. *in 52nd Specialists' Meeting of the Electromagnetic Wave Propagation Panel*, AGARD, Palma De Mallorca, Spain, 1993.

Livesey, N.J., J.W. Waters, R. Khosravi, G.P. Brasseur, G.S. Tyndall, W.G. Read, Stratospheric CH3CN from the UARS Microwave Limb Sounder, *Geophys. Res. Lett. 28,* 779-782, 2001.

Müller, H. S. P., S. Thorwirth, D. A. Roth, and G. Winnewiser., The Cologne Database for Molecular Spectroscopy, http://www.ph1.uni-koeln.de/vorhersagen/.

Ochiai, S., MAES, in the proceedings of the forward model workshop, Bremen, Apr., 1999.

Pickett, H. M., R. L. Poynter, and E. A. Cohen. JPL Molecular Spectroscopy,

http://spec.jpl.nasa.gov/.

Poynter, R. L. and H. M. Pickett. Submillimeter, millimeter and microwave spectral line catalog, *Appl. Opt., 24*, 2235, 1985.

Reburn, W. J., R. Siddans, B. J. Kerridge, S. Buehler, A. von Engeln, P. Eriksson, T. Kuhn, K. Kunzi, and C. Verdes, Critical Assesments in Millimetre-Wave Atmospheric Limb Sounding, *ESTEC Contract No.: 13348/98/NL/GD, Final Report, September*, 2000.

Rodgers, C. D., Retrieval of atmospheric temperature and composition from remote measurements of thermal radiation, *Rev. Geophys. and Space. Phys.,14*, 609-624, 1976.

Rodgers, C. D., Charactrization and error analysis of profiles retrieved from remote sensing measurements, *J. Geophys. Res., 95* (D5), 5587-5595, 1990.

Rodgers, C. D., *Inverse Methods for Atmospheric Sounding: Theory and Practise*, World Scientific Publ., Series on Atmospheric, Oceanic and Planetary Physics, 2000.

Rosenkranz, P. W., Water Vapor Microwave Continuum Absorption: A Comparison of Measurements and Models, *Radio Science, 33*, 919–928,1998.

Rothman, L. S., R. R. Gamache, A. Goldman, L. R. Brown, L. A. Toth, H. M. Pickett, R. L. Poynter, J-M.Flaud, and C. Camy-Peyret., The HITRAN database: 1986 edition, *Appl. Opt., 26*, 4058, 1987.

Rothman, L. S., R. R. Gamache, R. H. Tipping, M. A. H. Smith, D. Ch. Benner, V. Malathy Devi, J.-M. Flaud, C. Camy-Pyret, A. Perrin, A. Goldman, S. T. Massie, l. R. Brown, and R. A. Toth., The HITRAN molecular database: editions of 1991 and 1992, *J. Quant. Spectrosc. Radia. Transfer, 48*, 469, 1992.

Rothman, L. S., C. P. Rinsland, A. Goldman, S. T. Massie, D. P. Edwards, J.-M. Flaud, A. Perrin, V. Dana, J.-Y. Mandin, J. Schroeder, A. McCann, R. R. Gamache, R. B. Wattson, K. Yoshino, K. Chance, K. Jucks, L. R. Brown, V. Nemtchinov, and P. Varanasi., The HITRAN spectroscpic database and HAWKS (HITRAN Workstation): 1996 edition, *J. Quant. Spectrosc. Radia. Transfer*, 1996.

Verdes, C., S. Bühler, A. von Engeln, P. Eriksson, T. Kuhn, K. Künzi, The Retrieval of Data from Sub-Millimetre Limb Sounding, Part 1, *ESTEC Contract No.: 11979/97/NL/CN*, Final Report, September, 2000.

Wehr, T., S. A. Bühler, A. von Engeln, K. Künzi, and J. Langen Retrieval of Stratospheric Temperatures from Space Borne Microwave Limb Sounding Measurements *J. Geophys. Res., 103*, 25997-26006,1998.